

# Individual risk attitudes arise from noise in neurocognitive magnitude representations

Received: 23 August 2022

Accepted: 25 May 2023

Published online: 17 July 2023

 Check for updates

Miguel Barretto-García   <sup>1,2,6</sup>, Gilles de Hollander  <sup>1,3,6</sup>,  
Marcus Grueschow  <sup>1</sup>, Rafael Polanía  <sup>4</sup>, Michael Woodford  <sup>5</sup> &  
Christian C. Ruff  <sup>1,3</sup> 

Humans are generally risk averse, preferring smaller certain over larger uncertain outcomes. Economic theories usually explain this by assuming concave utility functions. Here, we provide evidence that risk aversion can also arise from relative underestimation of larger monetary payoffs, a perceptual bias rooted in the noisy logarithmic coding of numerical magnitudes. We confirmed this with psychophysics and functional magnetic resonance imaging, by measuring behavioural and neural acuity of magnitude representations during a magnitude perception task and relating these measures to risk attitudes during separate risky financial decisions. Computational modelling indicated that participants use similar mental magnitude representations in both tasks, with correlated precision across perceptual and risky choices. Participants with more precise magnitude representations in parietal cortex showed less variable behaviour and less risk aversion. Our results highlight that at least some individual characteristics of economic behaviour can reflect capacity limitations in perceptual processing rather than processes that assign subjective values to monetary outcomes.

Risk aversion is the tendency of human and non-human decision-makers to choose smaller certain options over larger risky ones<sup>1</sup>. While the population on average is risk averse, there is considerable variability in the individual strength of this tendency, and some people display risk-neutral or even risk-seeking behaviour<sup>2</sup>. Traditional economic theories account for risk aversion by the non-linear, concave shape of the utility function that maps monetary outcomes to subjective usefulness of wealth<sup>3</sup>. Such accounts thus conceptualize individual differences in risk aversion as differences in how the brain assigns subjective values to objective monetary outcomes. However, such theories fail to capture two key phenomena in real-life decision-making under risk<sup>4</sup>.

First, if utility functions are concave enough to account for risk aversion in laboratory choices involving very small amounts of money, then decision-makers should be risk averse even for gambles with very large potential gains and only moderate losses<sup>1</sup>. Human participants,

however, do not behave according to these assumptions. Second, many existing utility-based theories fail to explain the stochasticity in risky choice: Empirical evidence consistently shows that choices vary across repetitions of the same choice options<sup>4–6</sup>. While this phenomenon can be incorporated in models by simply adding a random error term to the utility function<sup>7</sup>, such an approach fails to explain mechanistically why this choice stochasticity arises and whether it reflects some fundamental properties of neural computations that may lead to systematic biases and irrationalities.

Despite these conceptual problems, dominant neurocomputational accounts of individual differences in risk attitudes have mainly focussed on identifying neural valuation processes that may correspond to the computations captured by the utility function. While consistent correlations have been found in various prefrontal and subcortical regions<sup>8,9</sup>, it is still unclear from these findings what properties

<sup>1</sup>Zurich Center for Neuroeconomics, Department of Economics, University of Zürich, Zurich, Switzerland. <sup>2</sup>Department of Neuroscience, School of Medicine, Washington University in St Louis, St. Louis, MO, USA. <sup>3</sup>University Research Priority Program ‘Adaptive Brain Circuits in Development and Learning’ (URPP AdaBD), University of Zurich, Zurich, Switzerland. <sup>4</sup>Decision Neuroscience Laboratory, Department of Health Sciences and Technology, ETH Zürich, Zurich, Switzerland. <sup>5</sup>Department of Economics, Columbia University, New York, NY, USA. <sup>6</sup>These authors contributed equally: Miguel Barretto-García, Gilles de Hollander.  e-mail: [gmguel@wustl.edu](mailto:gmguel@wustl.edu); [christian.ruff@econ.uzh.ch](mailto:christian.ruff@econ.uzh.ch)

of neural processing may give rise to the individual variation in how the brain assigns value. This is particularly unclear since these computations are often conceptualized as a final stage in the value construction process that draws heavily on information passed on from preceding sensory and cognitive processing<sup>10</sup>.

Here we test an alternative theoretical framework that explains risk aversion and stochasticity in risky choice not by idiosyncratic valuation processes, but as consequences of capacity restrictions and biases in the initial perception of the choice options. The core assumption of this framework is that even if decision-makers take risky choices rationally—and thus attempt to maximize the expected value of the payoffs from their choices—they do not have access to the objective information about the option payoffs but only to capacity-constrained internal representations of it<sup>6</sup>. That percepts of numerical magnitudes are noisy and subject to several biases—resembling those observed for lower-level sensory percepts—has been well established by decades of work in psychophysics. For example, perceptual judgements are stochastic (that is, vary across repetitions) when human decision-makers need to quickly estimate or remember the numerical magnitudes of a set of stimuli<sup>11,12</sup>. Moreover, in purely perceptual tasks, humans tend to underestimate (numerical) magnitudes more strongly when these become larger<sup>13</sup>. Related studies in perceptual neuroscience suggest that noise and biases in magnitude perception may be a direct consequence of the noisy and logarithmic way in which numerical magnitudes are encoded by neurons in parietal cortex<sup>12,14–18</sup>. This offers the intriguing possibility that from a neurocognitive perspective, individual differences in financial decision-making may (at least partially) originate from biased perception caused by properties of parietal magnitude processing, rather than exclusively from subjective valuation processes instantiated in prefrontal and subcortical brain areas.

Recent economic models of risky choice have started to adopt this perspective and have proposed that risk attitudes may arise from the imprecision in mental representations of magnitudes<sup>6,19</sup>. These models assume, in line with the literature on perceptual judgements<sup>13</sup>, that logarithmic coding of the payoff information and Bayesian integration with an individual's previous beliefs (shaped by more frequent exposure to smaller magnitudes) leads to more variable and systematically underestimated percepts for larger magnitudes<sup>13</sup>. This has the consequence that even a decision rule that is adapted to maximize expected payoffs can result in choices that show hallmark patterns of risk aversion, in a manner that depends systematically on the noisiness of the underlying magnitude representations<sup>6</sup>.

This perceptual account of risk aversion naturally accounts for two key empirical phenomena that utility-based models struggle to explain. First, it naturally follows that economic choices will be stochastic, given that they are based on noisy mental magnitude representations<sup>20</sup>. Second, the logarithmic compression of mental magnitude representations can explain why participants are risk averse even for arbitrarily small gambles<sup>1,21</sup>, since diminishing sensitivity for different payoffs should simply be a function of the log-ratio of potential payoffs (that is, the distance on a logarithmic scale), irrespective of overall magnitude<sup>20</sup>. Crucially, the perceptual account of risk aversion also makes the prediction that individual or situational differences in risk aversion should be negatively related to the precision of the mental magnitude representations currently used by the decision-maker<sup>13,20,22</sup>.

While these theories thus formalize how apparent risk aversion may emerge from biased perception and the noise in magnitude representations, empirical support for these theories is limited. In particular, the existing studies have fitted their model to a single economic choice task and have inspected the relation of the fitted parameters with the choice variability in the same dataset<sup>6,19</sup>. No study so far has examined such links across different tasks, or linked any of these behavioural measures of risk preferences to characteristics of the neural coding of magnitudes. It is therefore unclear whether an individual's risk aversion can indeed be traced back, in a mechanistic sense, to the acuity with

which her brain represents magnitude information, and whether the noisiness (or inversely precision) of these magnitude representations is a stable trait that can parsimoniously account for the way in which an individual takes both perceptual and financial choices.

Here, we provide this evidence, by measuring the precision of mental and neural magnitude representations in a purely perceptual magnitude task and testing how these neurocognitive measures of perceptual magnitude precision can account for individual risk-taking behaviour in different contexts with varying sensory noise. By using a single unifying model that captures principles of magnitude representations<sup>6,11</sup>, we can thus not only link risk aversion to estimates of behavioural precision of mental magnitude perception, but also to its neural substrate of numerical representations in the right parietal cortex, which we measure with functional magnetic resonance imaging (fMRI).

## Results

### The experiment

To test whether numerical acuity is an individual neurocognitive trait that (1) generalizes across perceptual and economic tasks and (2) determines individual differences in risk aversion, we devised an experiment comprising two sets of tasks. First, we presented a perceptual magnitude comparison task in the MRI scanner during which participants ( $n = 64$ ) had to indicate which of two coin clouds was more numerous (Fig. 1b). This task allowed us to obtain both behavioural<sup>11</sup> and neural measures<sup>23,24</sup> of numerical acuity. Then, in a second set of experiments outside the scanner, we presented two sets of risky-choice tasks to measure individual differences in risk aversion (Fig. 1b–d). In one half of the risky-choice trials, we presented payoff magnitudes as coin clouds (Fig. 1c) and thus in the same presentation format as also used for the perceptual task. In the other half of trials, we presented the payoffs symbolically using Arabic numerals (Fig. 1d). This allowed us to test whether individual differences in numerical acuity and risk aversion generalize across non-symbolic and symbolic settings, and whether risk aversion decreases if stimulus discriminability is increased (that is, from non-symbolic to symbolic presentation). This latter hypothesis follows from model predictions (below) that if internal noise in magnitude representations is reduced, any perceptual bias giving rise to risk aversion should also decrease. Variations in magnitude were matched across both risky-choice tasks, allowing explicit comparisons of precision between presentation formats (see Methods for details). Participants were not explicitly informed about the range of magnitudes before the experiment, but the possible payoffs were typical for the types of payoff given for experiments at our laboratory. To formally model behavioural data, we used a variant of a noisy logarithmic coding (NLC) model<sup>6</sup> that builds on established models of numerical cognition<sup>11,25</sup> and could be fitted to all choice tasks.

### A common model for perceptual and risky choice

We used the NLC model as the guiding framework to test the generalizability of numerical acuity across perceptual and risky-choice tasks (see Methods for more details). The NLC model posits that decisions maximize expected payoffs on the basis of the mean Bayesian posterior magnitude estimate, which systematically integrates the prior belief about the magnitude distribution and the noisiness of the internal representations of the current magnitudes at stake<sup>13</sup>. The model assumes that the brain represents the magnitudes of the risky payoff  $X$  and the certain payoff  $C$  by  $r_x$  and  $r_c$ , two noisy estimates modelled as samples from a Gaussian distribution of logarithmically encoded magnitudes,

$$r_x \sim N(\log X, v^2), r_c \sim N(\log C, v^2).$$

Perception is formalized as a Bayesian inference process that combines these internal estimates with a common prior,

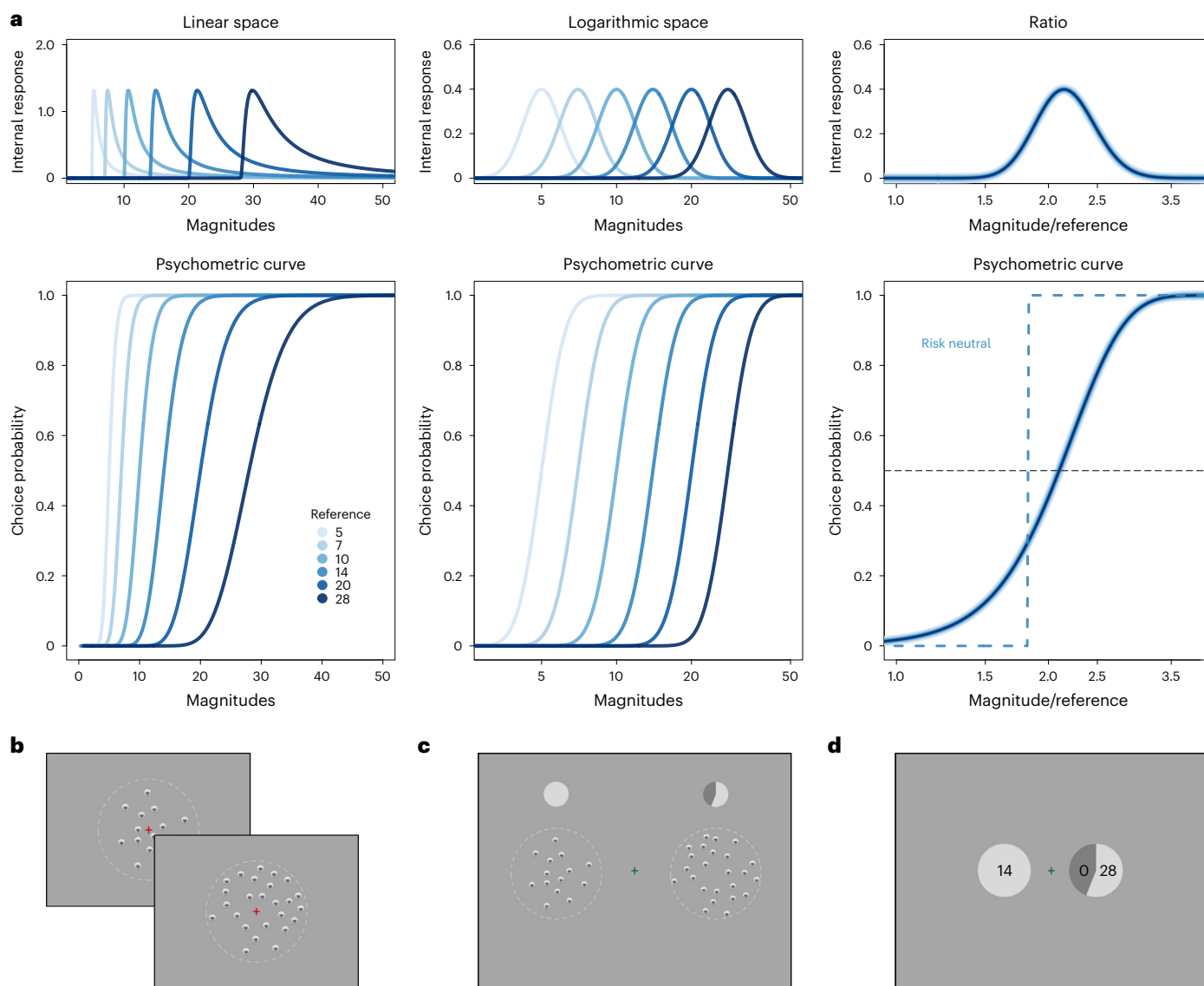


**Fig. 1 | The NLC model, experimental model and behavioural results.** **a**, The NLC model postulates that noisy magnitude encoding increases systematically with magnitude in linear space, represented as wider Gaussians as magnitudes increase (left, top). More variable choice behaviour increases in magnitude, expressed as shallower psychometric slopes (left, bottom). ‘Reference’ refers to the magnitude of the first set of coin clouds during the perceptual task or sure payoffs in risky choice. The Gaussians are encoded logarithmically, suggesting a lognormal noise distribution that is similar for all magnitudes in log space (middle, top), resulting in similar psychometric slopes (middle, bottom). These properties result in scale invariance in the log-ratio between magnitudes and reference (right, top) so that a single psychometric curve captures choice behaviour across all magnitudes (solid gradients of blue at right, bottom). Finally, the NLC model predicts that the precision in magnitude representation is directly related to risk aversion. Relative to the indifference point of a risk-neutral individual with precise representations (intersection of blue dashed step function and horizontal line at right, bottom), an individual with noisier

representations has shallower and right-shifted psychometric curves, resulting in only 30% of risky choices at the risk-neutral indifference point (intersection of solid psychometric function and dashed blue step function). The simultaneous change in slope and intercept is captured by the negative correlation between the precision of magnitude representation and risk aversion. **b**, Participants performed a numerical decision-making task inside the MRI scanner. On every trial, two clouds of 1-CHF coins were presented sequentially and participants had to indicate which of the two clouds contained more coins. We collected both neural and behavioural measurements to estimate the precision of the magnitude representations used for the task. **c,d**, Outside the MR scanner, participants took risky choices in which they had to choose either a risky gamble or a sure offer. We visually displayed the potential payoffs of offers as either non-symbolic coin clouds similar to the perceptual task (**c**) or symbolic Arabic numerals (**d**). Probabilities were presented as pie charts. We fixed the probabilities at  $p = 0.55$  in favour of the risky monetary offer.

$\log X, \log C \sim N(\mu, \sigma^2)$  that specifies the distribution of numerical magnitudes the decision-maker expects to encounter in the testing environment. Central to the model is the individual parameter  $\nu$  that represents the noise of the internal representations of numerical magnitudes. The parameter,  $\sigma$ , on the other hand, is the width of the prior that accounts for the dispersion of numerosities that the decision-maker deems plausible. The decision process involves

optimization of the expected payoff on the basis of the mean posterior magnitude estimate

$$\mathbb{E}[X|r] = \exp(\alpha + \beta r_x), \mathbb{E}[C|r] = \exp(\alpha + \beta r_c)$$

where  $\beta = \frac{\sigma^2}{\sigma^2 + \nu^2}$  is a multiplier that determines the weight of the noisy estimate  $r$  relative to the prior and  $\alpha = (1 - \beta)\mu$  is a constant, where  $\mu$ ,

$\sigma^2$  determines the location of the lognormal prior distribution. The larger the noise in mental magnitude representations  $r$  (reflected by a larger  $v$ ), the shallower and more regressive the expected-value function over the payoffs.

With these underlying representational mechanisms, we can derive a psychometric function and thus the probability with which the decision-maker chooses the risky option with payoff  $X$  over the safe option with payoff  $C$ :

$$\Pr(\text{choose risky}|X, C) = \Phi\left(\frac{\log(X/C) - \beta^{-1} \log p^{-1}}{\sqrt{2v}}\right)$$

where  $\Phi(\cdot)$  is the standard normal cumulative density function that maps the choice of the risky option with payoff  $X$  over the sure option with payoff  $C$  into the probability  $\Pr(\text{choose risky}|X, C)$ , and  $p$  is the probability of the risky payoff. In our task,  $X$  and  $C$  represent the objective magnitudes of the second- and first-coin clouds during the perceptual magnitude task and the magnitudes of the risky and certain payoffs during the risky choice task, respectively. We can conveniently estimate the NLC parameters using a standard probit model,

$$\Pr(\text{choose risky}|X, C) = \Phi\left(\gamma \log\left(\frac{X}{C}\right) - \delta\right).$$

This parametrization is equivalent to the NLC via the relationships in the slope,  $\gamma = \frac{1}{\sqrt{2v}}$ , and intercept,  $\delta = \left(\frac{\beta^{-1} \log(p^{-1})}{\sqrt{2v}}\right)$ .

The following are key measures for our analysis. First, the slope  $\gamma$  captures the precision in mental magnitude representations (the inverse of noise,  $\sqrt{2v}$ ) while the intercept  $\delta$  captures the indifference point between both options. More precisely, the indifference point  $\theta = \exp\left(\frac{\delta}{\gamma}\right)$  is where the individual is indifferent in choosing between  $r_x$  and  $r_c$ . A crucial corollary of locating the indifference point is the ability to index risk aversion as risk-neutral probability  $\pi_{\text{risk}} = \exp\left(-\frac{\delta}{\gamma}\right)$ , the probability level at which the decision-maker should be indifferent between the risky and the safe option. The NLC prescribes that a decision-maker with imprecise mental magnitude representations should show  $\pi_{\text{risk}} < 0.55$  and thus behave as if the probability of receiving the risky payoff is smaller than it actually is (which, by definition, is apparent risk aversion). The ‘risk-neutral’ probability during the perceptual magnitude comparison task, on the other hand, should trivially be  $\pi_{\text{perceptual}} = 1$ , since both options are associated with the same degree of (subjective) uncertainty.

### The NLC model is a better account for risky-choice behaviour than established utility-based models

As a necessary condition, we established that our perceptual account of risk aversion can capture the empirical data at least as well as dominant economic theories. We used formal techniques to compare the NLC model’s fit to the risky choice data with the fits of classical decision-making theories such as expected utility maximization, cumulative prospect theory and salience theory, all in logit and probit form (see Methods for details). The formal model comparison revealed that the NLC model fit the data best, since it always had the lowest deviance information criterion (DIC), regardless of presentation format (Extended Data Fig. 1a,b). This underlines the plausibility of the neurocognitive operations formalized in the model.

### Decoding magnitude from neural activity

The NLC model assumes that both numerical magnitudes and potential payoffs are represented in the same noisy logarithmic manner. This builds on established neuroscientific findings that neural population activity in numerical parietal cortex (NPC) is tuned to

numerical magnitudes, with the width of neural tuning reflecting moment-to-moment noisiness (or inversely, precision) of neural magnitude representations across repeated stimuli<sup>23</sup>. We directly tested these implicit, mechanistic links between neural and cognitive magnitude representations, by investigating the relationship between behavioural precision in the perceptual magnitude task and the fidelity of parietal magnitude representations measured by blood-oxygen-level-dependent (BOLD)-fMRI during the perceptual decision-making task<sup>24</sup>. To this end, we fitted a numerical population receptive field (nPRF) model that assumes that every patch of (parietal) cortex responds to a specific part of the number line, with its response profile characterized as a Gaussian kernel on the logarithmic number line (Fig. 2a)<sup>15,23</sup>. We plotted the centre of the tuning curve for every vertex and averaged across the 64 participants on a standard brain surface (fsaverage), and thresholded this map by the average explained variance  $R^2$  of the nPRF model (Fig. 2b).

We found that large regions in parietal cortex were sensitive to numerical magnitude stimuli. Many of these were topographically organized according to their most-preferred magnitude (Fig. 2b), thus replicating related findings of topographic neural magnitude representations in parietal cortex<sup>15,16,23</sup>. Given established links between neural decoding accuracy in the (right) intraparietal region and task performance<sup>18,26</sup>, we manually segmented a region between the intraparietal sulcus (IPS) and the precentral sulcus that was both magnitude-sensitive and showed topographic organization. The region was qualitatively similar to the NPC1, NPC2 and NPC3 regions defined by Haye et al.<sup>15,23</sup>; we therefore labelled it the ‘NPC’ region. Notably, it also included both the lateral and ventral parietal cortex reported in previous work<sup>18,26</sup>. Even though behaviourally relevant magnitude representations have been reported to be right lateralized<sup>18,26</sup>, our goal for the initial mapping analyses was to have two unbiased hemispheric regions of interest that included all earlier reported regions and let our Bayesian decoder decide on a person-to-person basis which subregions (that is, vertices) were most informative. We chose this integrated approach over the use of multiple statistical tests for many individual regions of interest, since it has higher statistical sensitivity as needed for our study on individual differences in  $n = 64$  people.

The neural magnitude representations in this NPC area were indeed highly specific, as we ascertained by inverting the encoding model and decoding the presented stimulus from NPC-BOLD activity patterns in held-out data. This worked better than chance (16.67%) in 56 out of 64 participants in left NPC (average accuracy 23.6%, s.d. 5.4%) and 60 out of 64 participants in right NPC (average accuracy 23.8%, s.d. 5.2%). These accuracies were significantly different from chance-level decoding (16.67%) at the group level ( $t(63) = 10.4$ ,  $P < 0.001$ , Cohen’s  $d = 1.30$ , 95% confidence interval (CI) of (0.22, 0.25) for left NPC and  $t(63) = 11.0$ ,  $P < 0.001$ , Cohen’s  $d = 1.36$ , 95% CI = (0.23, 0.25) for right NPC). To make our results comparable to a recent study of perceptual accuracy<sup>18</sup>, we also computed the accuracy with which our decoder picked the right stimulus pair from all possible pairs. The average pairwise decoding accuracy was 59.1% for the left NPC and 59.0% for the right NPC. This is higher than the 56.7% accuracy reported by the previous study<sup>18</sup>, even though those authors tested within a smaller number of stimulus categories (two sets of three). We speculate that our increased decoding accuracy might be explained by the use of a model-based encoding-decoding framework that explicitly accounts for the non-linear tuning functions in parietal cortex that have been found in studies in both human and non-human primates<sup>12,23,27</sup>. Linear multivariate pattern analysis methods, such as the support vector machine used in the previous study<sup>18</sup>, may be less well suited to decode such non-linear tuning functions. Misclassified stimuli were usually classified as a stimulus relatively close in magnitude (Fig. 2d). However, in line with the notion that magnitude representations may be right lateralized<sup>18</sup>, the average within-participant correlation between the presented magnitude and the mean decoded posterior was twice as

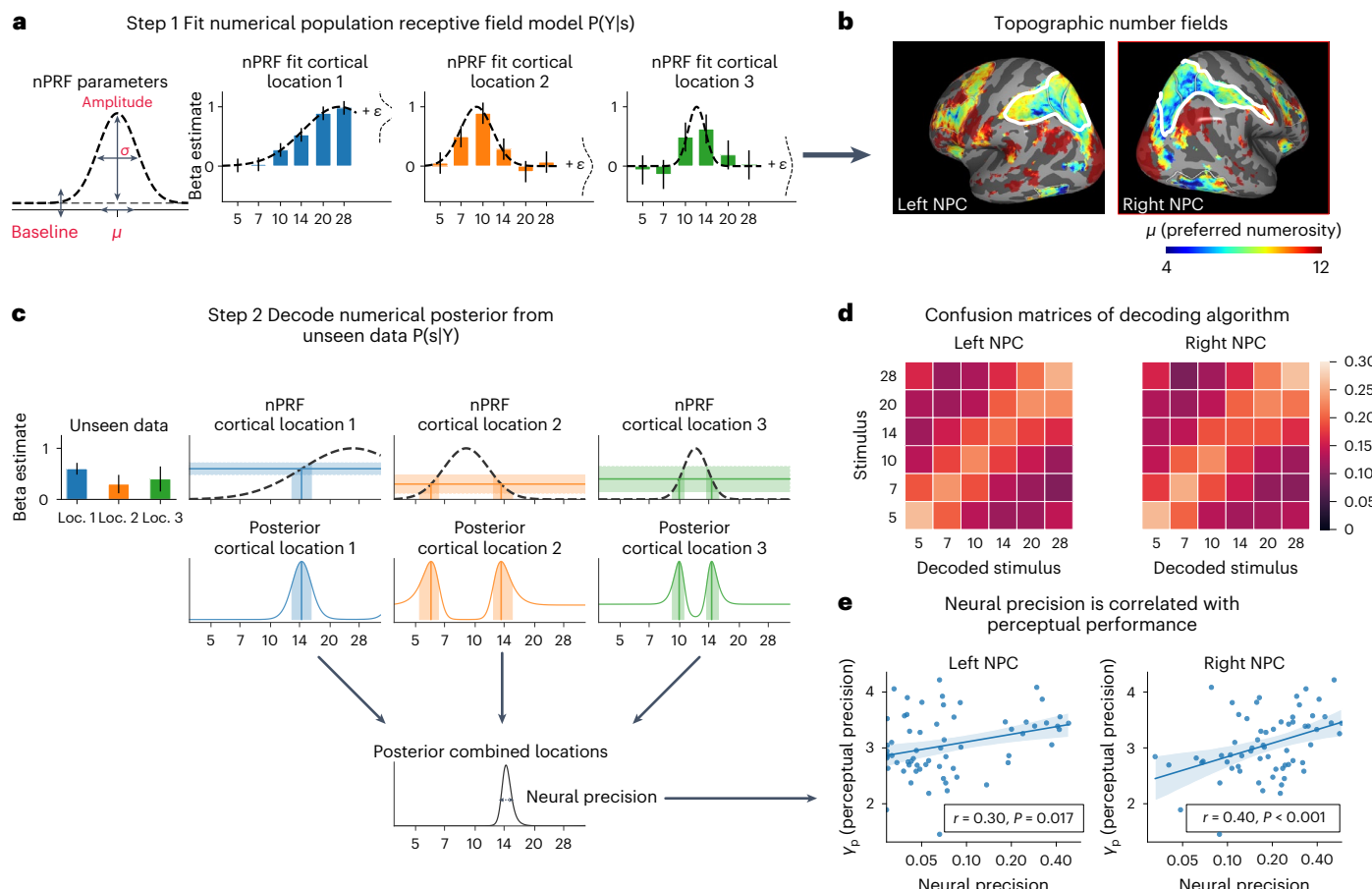


**Fig. 2 | Neural magnitude representations in parietal cortex.** **a**, Illustration of the nPRF model. Bar plots represent hypothetical mean BOLD response to different magnitudes and their standard error. Dotted lines are Gaussian kernels fitted to these response profiles.  $P(Y|s)$  defines the encoding model, which maps stimuli to voxelwise time series plus their multivariate noise distribution ( $Y$ ). We refrain from presenting real data since we collected data for 64 participants, each with hundreds of IPS vertices, precluding us to concisely show representative data. The lognormal nPRF model has been validated before by Harvey et al.<sup>15,23</sup>. **b**, In line with earlier work, we found topographic organization of different numerosity preferences in bilateral NPC. **c**, Illustration of decoding using Bayesian model inversion. Bar plots (left, top panel) are hypothetical estimates of BOLD activation responses to unseen stimuli and their standard errors (shaded area).  $P(s|Y)$  represents the inversion of the encoding model and maps trialwise, multivariate BOLD activation patterns in IPS to posterior distributions over possible magnitudes. Bayesian inversion of the PRF model yields a posterior distribution over possible stimulus magnitudes, given the BOLD activity pattern. Our measure of imprecision in the neural magnitude representation is the standard deviation of this posterior (middle panel). Peaks of the posterior's

bimodal distribution (solid vertical lines, middle panel) represent the most likely stimulus, according to the BOLD activation in a single cortical location (loc.) with a single receptive field (solid horizontal lines, top panels). Shaded areas correspond to the standard deviations of the beta estimates in the left panel. Multivariate information is integrated into a single posterior that quantifies the probability of possible magnitudes eliciting the multivariate BOLD response pattern (bottom panel). **d**, Confusion matrices show, for every stimulus category (rows), how often the decoder classifies trials as one of six possible stimulus categories (columns). All entries on the diagonal correspond to correctly classified stimulus categories, whereas off-diagonal categories represent misclassifications. Diagonal entries are always higher than the off-diagonal entries and entries near the diagonal are usually higher than entries further from the diagonal. More extreme magnitudes are decoded with higher fidelity. **e**, The neural precision,  $\frac{1}{s.d.}$  of the decoded posteriors ( $n = 64$ ) is significantly correlated with the precision of mental magnitude representations during the perceptual decision-making task, as indexed by the parameter  $\gamma_{\text{perceptual}}$ .  $P$  values were estimated from one-sided Pearson correlations.

high for right NPC ( $r(239) = 0.216$ ) than for left NPC ( $r(239) = 0.117$ ) (paired  $t$ -test:  $t(63) = 6.17, P < 0.001$ , Cohen's  $d = 0.83$ , 95% CI = (0.07, 0.13)). Indeed, the standard deviations of the decoded posterior were also smaller (right, 6.9 versus left, 17.4).

### Behavioural differences in numerical acuity relate to the precision of neural magnitude representations

Crucially, our neural model allowed us to not only identify neural magnitude representations in parietal cortex, but also to derive a standard index of how precisely magnitudes are represented by neural population activity<sup>24,28</sup>. We can measure each individual's general degree of neural precision in encoding magnitudes by the mean precision,  $\frac{1}{s.d.}$  of the posterior across all stimulus categories (Fig. 3e, red arrow).

The NLC model implicitly assumes that its measure of precision in mental magnitude representations should reflect the precision of the corresponding neurobiological representations. Consistent with this hypothesis, we found significant positive correlations between each participant's performance on the perceptual task (measured by the precision parameter,  $\gamma_{\text{perceptual}}$ ) and the index of general neural precision ( $\frac{1}{s.d.}$  of decoded posteriors, averaged over all six stimulus categories) in right NPC ( $r_{\text{right}}(62) = 0.404, P < 0.001$ , 95% CI = (0.180, 0.590); Fig. 2e) and to a certain extent also in left NPC ( $r_{\text{left}}(62) = 0.300, P = 0.0168$ , 95% CI = (0.06, 0.51)). This confirms a strong link between the noise in neural representations of numerical magnitudes and variability in performance during magnitude perception, in particular for right NPC. Congruent with this apparent right

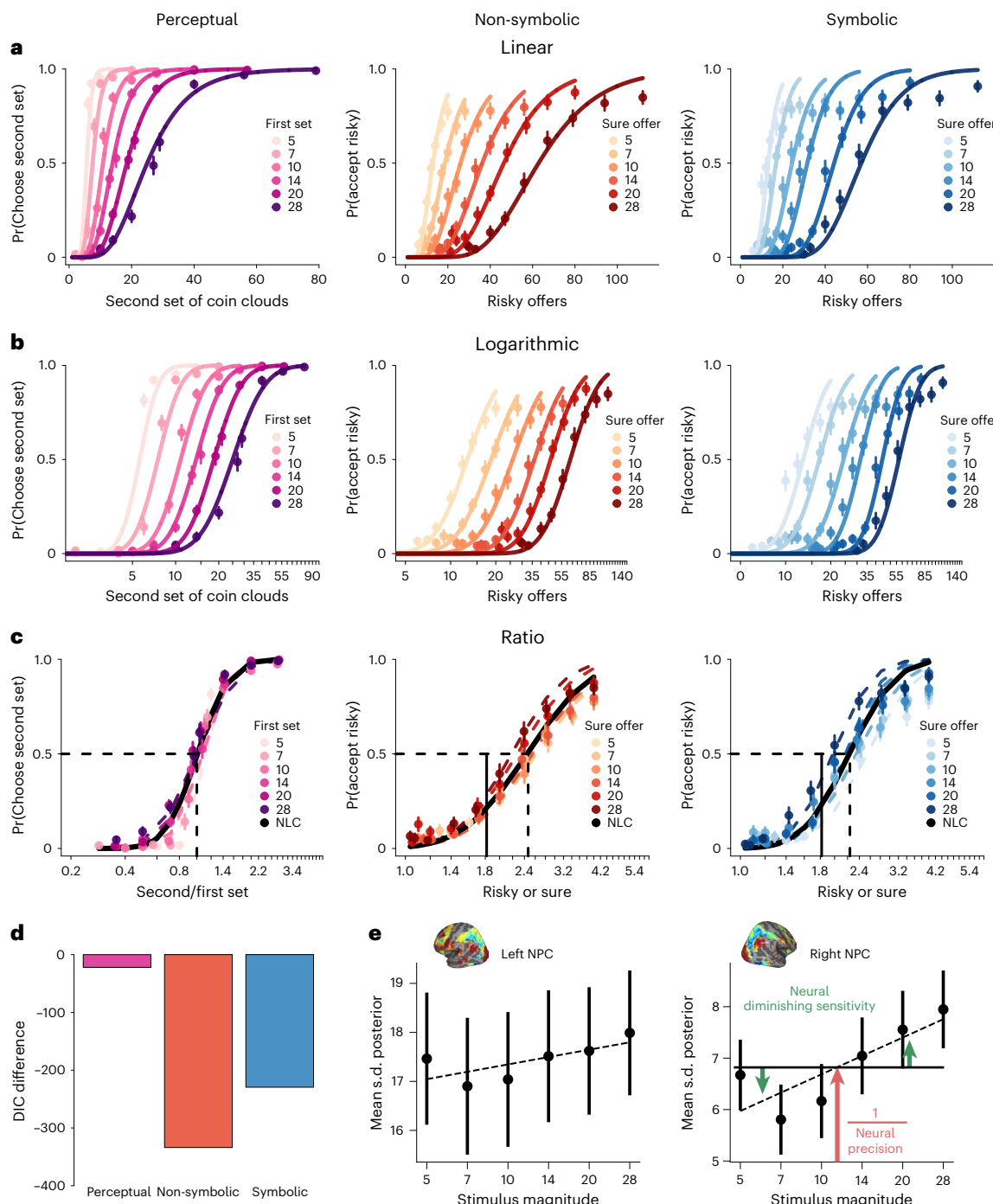


**Fig. 3 | Domain-generality of scale invariance across perceptual and risky-choice tasks.** **a,b**, Observed probabilities ( $n = 64$ ) of choosing the second stimulus for magnitude judgements (left) or the risky option (middle and right) plotted in linear space (**a**) and logarithmic space (**b**), separated by visual display type (non-symbolic payoffs, middle and symbolic payoffs, right). The six psychometric curves correspond to the magnitudes of the first stimulus arrays in the magnitude task or sure offers in the risky-choice task. Fits used linear and log models using a subset of the magnitude and risky offers as a subset of their respective reference magnitudes and/or offers. **c**, Observed choice probabilities plotted as the ratio of the second- and first-coin cloud magnitudes (magnitude) or risky and sure payoffs (risky-choice). Initial inspection similar psychometric curves irrespective of task domain or visual display, suggesting common logarithmic magnitude coding across tasks. Moreover, the six psychometric slopes stack over each other, and we can fit a single psychometric curve (solid black curve) to account for all choice probabilities in all task domains and visual

displays. The coloured dashed psychometric curves used the NLC to fit a subset of offer or magnitude distributions conditional on the reference. The intersection of the horizontal and vertical dashed lines represents the point where the individual is indifferent between choosing the risky and sure payoffs. Data points are pooled across participants and error bars on each circle represent s.e.m. The solid vertical line represents the indifference point of a risk-neutral individual. **d**, DIC difference between the best model (the NLC with one slope parameter for all experimental conditions) and the competing unrestricted model with separate slopes for each combination, for all types of choice and display. **e**, Dispersion (s.d.) of the decoded posteriors ( $n = 64$ ) increases as a function of stimulus magnitude—a hallmark of scale invariance. We quantified, on a person-to-person basis, both average neural precision ( $\frac{1}{\text{s.d.}}$  of the posterior) across magnitudes and neural diminishing sensitivity, the extent to which neural representations get noisier as a function of stimulus magnitude. Error bars are s.e.m. across participants.

lateralization, earlier studies had found similar brain–behaviour relationships mainly for the right parietal cortex<sup>18,26</sup>.

### Evidence that similar logarithmic magnitude representations may guide both perceptual and risky choices

A central assumption of the NLC model is that noisy logarithmic magnitude representations should be scale invariant, which should be evident in at least two ways: (1) the probability of choosing the second coin cloud in the perceptual task and the risky gamble in the risky choice task should be determined by the log-ratio of the two magnitudes,  $\frac{X}{C}$ , rather than by their absolute magnitudes (Fig. 1a, middle and right); and (2) the noise in internal magnitude representations should increase with magnitude (Fig. 1a, left). To visually test for these hallmark signs of the representations assumed by the NLC model, we plotted the probabilities of judging the second set of coins larger than the reference stimulus (Fig. 1b) or choosing the risky gamble over the sure gamble (Fig. 1c,d) in both linear (Fig. 3a) and log (Fig. 3b) spaces. We used a hierarchical Bayesian framework (Methods) to fit the psychometric curves. This approach models individual-level variability explicitly when estimating group-level parameters. Initial visual inspection already shows that in linear space, the choice curves vary differently and are skewed. But when replotted on a log scale or a log-ratio scale, the slopes ( $y$ ) become very similar to each other (Fig. 3c), suggesting scale invariance. We also formally tested for scale invariance by comparing model fits of a single NLC psychometric curve to an unrestricted model that separately fitted six such psychometric curves for each of the six reference stimuli. Model comparisons revealed that the NLC model's single psychometric curve fitted to all magnitude stimuli explained the data far better than the unrestricted model (Fig. 3d), thus confirming scale invariance in the choice data and replicating previous results<sup>6</sup>. Note that the aggregate choice curves for the risky choice task never reach a choice proportion of 1, not even for the most attractive risky offers. However, 35 participants in the non-symbolic task and 40 participants in the symbolic task did choose the risky option in 100% of the trials for the highest offers (Extended Data Figs. 2 and 3). The remaining participants had relatively shallow choice curves and were, in particular, risk averse (Extended Data Figs. 2 and 3). This suggests that lapses<sup>29</sup> did not occur often and are thus unlikely to influence our further results.

Crucially, we also tested whether scale invariance applies to the neural magnitude representations identified with our encoding and/or decoding approach. In addition to the precision of neural representations across all magnitude levels (mean precision,  $\frac{1}{\text{s.d.}}$ , Fig. 3e, red arrow), we could also derive a measure of neural diminishing sensitivity. The slope of the regression of the decoded posterior's mean s.d. on stimulus magnitude, indexing how strongly, in a given individual, neural representations become less precise with increasing magnitudes (Fig. 3e, green arrows). Note that the first measure (neural precision) can be contaminated by non-cognitive factors unspecific to magnitude coding, such as size of the cortical sheet, neurovascular coupling, attention, and head movement<sup>30</sup>. The second measure (neural diminishing sensitivity) is less likely to be affected by such unspecific general noise factors, which presumably do not vary systematically with trial-wise stimulus magnitudes. Thus, for participants who exhibit imprecision specifically in the neural coding of magnitudes, and for whom this coding follows scale invariance, we expect the slope of decoding uncertainty across magnitude levels to be systematically higher, on top of any general neural noise also affected by non-cognitive noise sources.

Confirming neural diminishing sensitivity, we found that the larger the stimulus magnitude, the noisier the neural magnitude representation in left NPC (Fig. 3e, left panel, repeated measures correlation,  $r(319) = 0.23$ ,  $P = 0.001$ , 95%CI = (0.13, 0.34)), but this effect was much more pronounced in the right NPC (Fig. 3e, right panel,

$r(319) = 0.43$ ,  $P < 0.001$ , 95%CI = (0.34, 0.52)). These results again confirmed an apparent right lateralization for the neural locus of the approximate numerosity judgements, of which diminishing sensitivity is a hallmark phenomenon. In sum, the initial analyses of the parietal number representations show that, compared to the left NPC, number representations in the right NPC (1) are easier to decode, (2) more closely relate to individual differences in numerical acuity and (3) show stronger diminishing sensitivity. We thus opted to use neural recordings from the right NPC to derive the index of the precision of neural magnitude representations for all subsequent analyses on the link between risky choice and NPC activity.

### The NLC captures how noise in magnitude representations mechanistically leads to perceptual bias and risk aversion

A crucial implication of the NLC model is that it specifies the link between magnitude representation noise and the point at which participants become indifferent between the choice options. Specifically, the noisier the magnitude representation, the more influential the prior distribution becomes and the more the magnitude of the risky option will be underestimated compared to the safe option (see Extended Data Fig. 4 for more detail). In pure magnitude perception, where it is known a priori that there is no outcome uncertainty, the individual's indifference point should lie around  $\theta_{\text{perceptual}} \approx 1$ , the point where both magnitudes are equal,  $X = C$ . In risky choice, the objective outcome probability  $P = 0.55$  should lead to an indifference point  $\theta = \frac{X}{C} = \frac{1}{0.55}$  for perfectly precise magnitude representations ( $v = 0$ ). However, any degree of noise  $v > 0$  will shift the indifference-point threshold to  $\theta > \frac{1}{0.55}$  and thus to apparent risk aversion, since people become indifferent only for larger  $X$  at the given  $P$ . This prediction by the NLC should be evident by the location of the probit intercept, which should not be statistically different from zero ( $\delta = 0$ ) for perceptual judgements but greater than zero ( $\delta > 0$ ) for risky choice.

Indeed, population-level posterior distributions of the intercept estimated with a hierarchical Bayesian framework were all in line with model prescriptions (Extended Data Fig. 5a,  $\delta_{\text{perceptual}} = -0.168$ ,  $P_{\text{MCMC}} = 0.204$ ; Extended Data Fig. 5b,  $\delta_{\text{non-symbolic}} = 2.41$  and  $\delta_{\text{symbolic}} = 2.97$ ,  $P_{\text{MCMC}} < 0.001$  for both measures). Post hoc tests showed no evidence of an effect for the indifference-point threshold in perceptual magnitude (Extended Data Fig. 5c,  $\theta_{\text{perceptual}} = 0.95$ ,  $P_{\text{MCMC}} = 0.204$ ) while the indifference points for risky payoffs across visual presentation formats were greater than  $\frac{1}{0.55}$  (Extended Data Fig. 5d (left panel),  $\theta_{\text{non-symbolic}} = 2.46$  and  $\theta_{\text{symbolic}} = 2.24$ ,  $P_{\text{MCMC}} < 0.001$  for both measures). Given that previous work<sup>14</sup> only tested the NLC within a single economic choice task, our study provides new evidence that the mechanisms embedded in the model can flexibly account for biases in both perceptual and risky economic choices.

### Similar magnitude representations guide risky choice across visual display formats and individuals

The NLC model defines the noisiness of mental magnitude representations  $v$  as a function of  $y$ , the precision with which individual decision-makers can mentally differentiate magnitude stimuli. At the same time, the NLC model assumes that choice behaviour should independently be influenced by different beliefs about the variability of magnitudes in the environment (measured by the width of the prior,  $\sigma$ ) as well as by sensory noise in the stimulus display (which should also affect the precision of magnitude representations). However, these core features of the NLC model have thus far remained untested, since previous studies have related the risk-neutral probability  $\pi$  (which is smaller for larger risk aversion) to the precision in mental magnitude representation  $y$  only for parameters fitted to a single economic task with only one type of visual display (for example, symbolic payoffs). If  $y$  really reflects an individual trait, then the relationship between  $\pi$  and  $y$  should generalize across tasks and variations in sensory noise; but the sensory noise level should nevertheless have systematic effects on risk aversion.

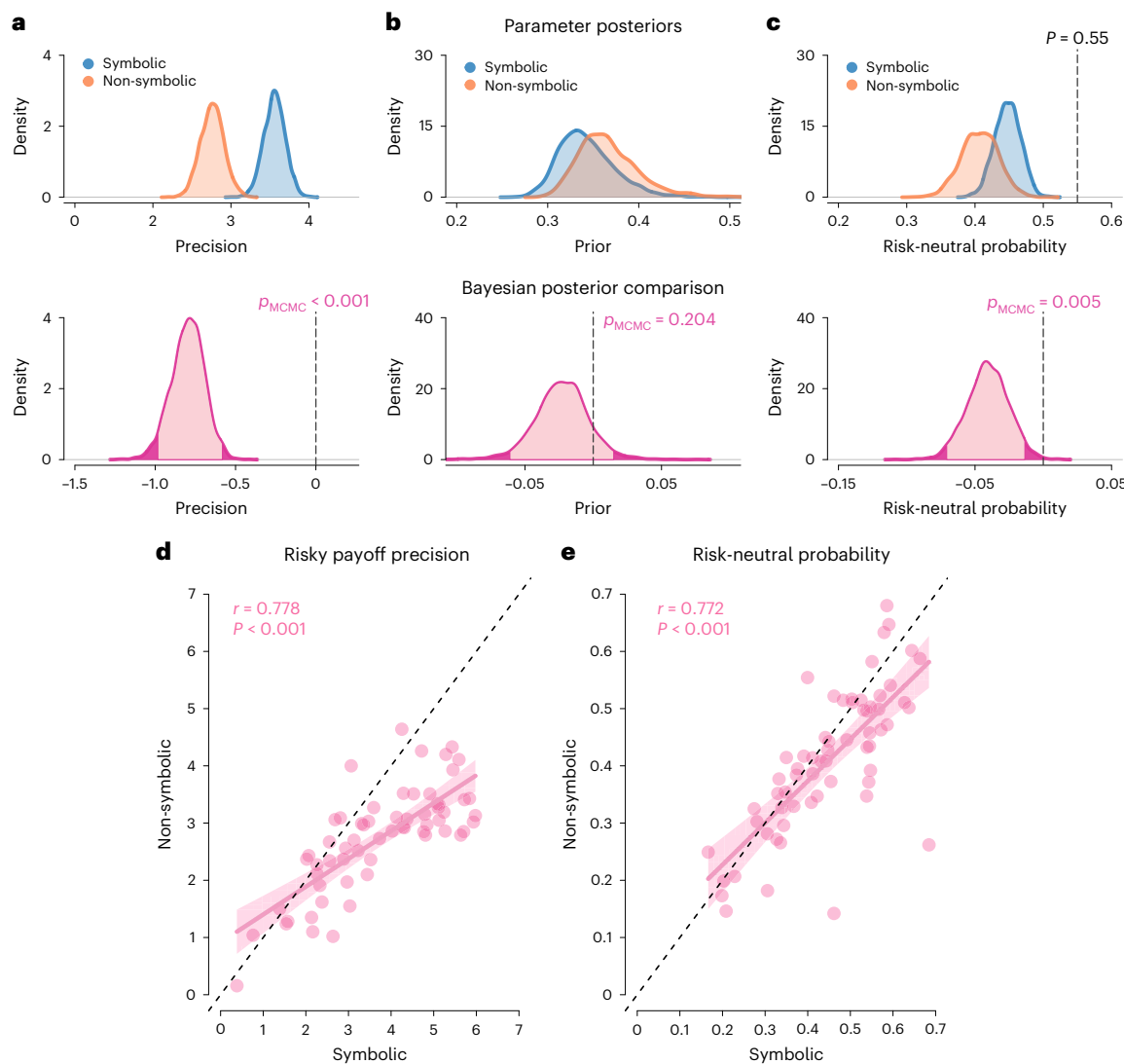


**Fig. 4 | Noise in mental magnitude representations is individually robust across different types of visual display of risky prospects.** **a–c**, Population posterior distributions of risky payoff precision (**a**), the prior (**b**) and risk aversion (**c**) for risky symbolic payoffs and risky non-symbolic payoffs in risky-choice behaviour. Top plots are distributions for both types of display (symbolic payoffs in blue, non-symbolic payoffs in yellow) while bottom plots are distributions of differences between display formats (in pink). Bayesian  $P$  values were calculated. The light-shaded mass of the highest density interval covers 95% of the posterior distribution while the dark-shaded tail ends represent 5% of the posterior distribution. In top plots, the vertical dashed line represents the ‘rational’ risk-neutral probability,  $P = 0.55$ , whereas in bottom plots, it represents

zero. Representations were more precise during symbolic payoffs,  $\gamma_{\text{symbolic}}$ , than non-symbolic payoffs,  $\gamma_{\text{non-symbolic}}$ . This is reflected as larger risk aversion (or lower risk-neutral probability) for non-symbolic payoffs,  $\pi_{\text{non-symbolic}}$  relative to symbolic payoffs,  $\pi_{\text{symbolic}}$ . There is no difference between the priors,  $\sigma_{\text{non-symbolic}}$  and  $\sigma_{\text{symbolic}}$ . **d,e**, Individual measures of risky payoff precision (**d**) and risk-neutral probability (**e**) for symbolic and non-symbolic payoffs ( $n = 64$ ) are related: the two measures are positively correlated. The shaded area around the regression line represents 95% confidence intervals. The black dashed line represents the identity line.  $P$  values were estimated from one-sided Pearson correlations.

We tested this hypothesis by comparing the same risky choices presented either symbolically as numbers or non-symbolically as coin clouds (Fig. 1c,d). First, we predicted that individuals should be more risk averse when faced with non-symbolic payoffs, since symbolic payoffs are easier to identify and map onto mental magnitude representations (note that the distribution of stimulus magnitudes was identical for non-symbolic and symbolic payoffs, so the prior between the two stimulus displays should be no different). Second, we expected that we will replicate previous results of a positive and non-linear relationship between risky payoff precision  $\gamma_{\text{risky}}$  and risk-neutral probability  $\pi$  (ref. 6) for both display formats, and that each individual's magnitude precision will be related across the two visual display formats.

Our results confirm all these predictions. Population-level posterior distributions of the corresponding parameters confirmed that representations of non-symbolic payoffs were less precise than symbolic ones (Fig. 4a,  $\gamma_{\text{non-symbolic}} = 2.76$ ,  $\gamma_{\text{symbolic}} = 3.56$ ,  $P_{\text{MCMC}} < 0.001$ ) and that the individual indifference points between risky and sure gambles were indeed higher during non-symbolic payoff presentations ( $\theta_{\text{non-symbolic}} > \theta_{\text{symbolic}}$  (Extended Data Fig. 5d (right panel),  $P_{\text{MCMC}} = 0.005$ ). As expected given the noisiness of mental magnitude representations, risk aversion was substantial for both display formats (Fig. 4c (top-right panel),  $\pi_{\text{non-symbolic}} = 0.408$ ,  $\pi_{\text{symbolic}} = 0.448$  are less than 0.55,  $P_{\text{MCMC}} < 0.001$ ) and risk-neutral probabilities were indeed systematically smaller (corresponding to more risk aversion) for non-symbolic payoff display formats (Fig. 4c (middle-right panel),

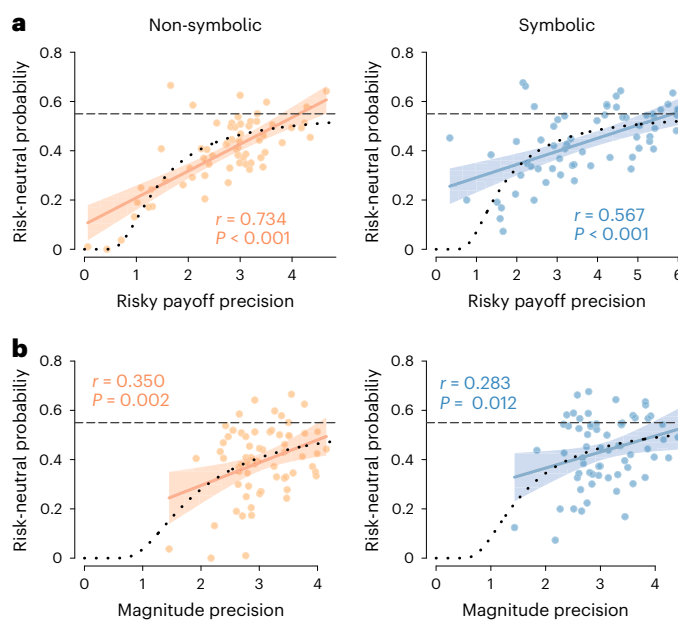


**Fig. 5 | The precision of mental magnitude representations systematically relates to individual risk attitudes.** **a,** The estimated precision of the representation of potential payoffs,  $\gamma_{\text{non-symbolic}}$  and  $\gamma_{\text{symbolic}}$ , and the index of risk aversion (measured by individual risk-neutral probability,  $\pi_{\text{non-symbolic}}$  and  $\pi_{\text{symbolic}}$ ) ( $n = 64$ ) are related across all visual displays. The curved dotted line is the prediction from the psychometric model linking the relationship between risk payoff precision and risk-neutral probability under the assumption of a common lognormal prior. The common prior we used to fit the curve for each presentation format ( $\sigma_{\text{non-symbolic}}$  and  $\sigma_{\text{symbolic}}$ ) was estimated using the non-linear relationship formalized by the NLC model (Methods). Participants (represented as circular dots) whose risk-neutral probability are on the horizontal dashed line are risk-neutral while participants below the dashed line are risk averse and participants above the dashed line are risk-seeking. **b,** The estimated precision of magnitude representations during perceptual decision-making and individual risk attitudes ( $n = 64$ ) are related, consistently across visual display type. The shaded area around the regression line represents 95% confidence intervals. The horizontal dashed lines represent risk-neutral behaviour while the curved dotted line is now the prediction linking risk-neutral probability with magnitude comparison precision.  $P$  values were estimated from one-sided Pearson correlations.

$P_{\text{MCMC}} = 0.005$ ). These differences in the indifference point and risk-neutral probability did not appear to reflect different beliefs about stimulus magnitude distributions, since the estimated priors were not different between non-symbolic and symbolic payoffs (Fig. 4b,  $\sigma_{\text{non-symbolic}} = 0.366$ ,  $\sigma_{\text{symbolic}} = 0.343$ ,  $P_{\text{MCMC}} = 0.204$ ).

We also compared the precision of mental representations between both tasks. Given the experimental set-up, one would expect that the magnitude representations for the non-symbolic coin clouds in the perceptual magnitude task should be less precise than for the symbolic payoffs in the risky choice task, but more precise than for the non-symbolic risky payoffs. This is because internally representing non-symbolic risky payoffs requires the integration of both coin cloud stimuli and probability information. Group-level posterior distributions confirmed this conjecture ( $\gamma_{\text{perceptual}} > \gamma_{\text{non-symbolic}}$ ,  $P_{\text{MCMC}} = 0.008$ , Extended Data Fig. 6b (left panels) and  $\gamma_{\text{symbolic}} > \gamma_{\text{perceptual}}$ ,  $P_{\text{MCMC}} < 0.001$ , Extended Data Fig. 6b (right panels)).

In line with our second hypothesis—that common magnitude representations are used during both display types, but are subject to differing sensory noise—we found significant positive correlations across visual

display types between the risk precision measures (Fig. 4d,  $r_y(62) = 0.778$ ,  $P < 0.001$ ,  $CI = (0.657, 0.859)$ ), the measures for the indifference point (Extended Data Fig. 5e,  $r_\theta(60) = 0.703$ ,  $P < 0.001$ ,  $95\% CI = (0.549, 0.810)$ ) and the risk-neutral probabilities (Fig. 4e,  $r_\pi(62) = 0.772$ ,  $P < 0.001$ ,  $95\% CI = (0.649, 0.855)$ ). These results were also observed with non-parametric and robust statistical tests (Supplementary Table 1). Finally, we correlated the risk-neutral probability  $\pi$  with precision  $\gamma$  for both visual displays (Fig. 5a). The significant positive correlations ( $r_{\text{non-symbolic}}(62) = 0.734$ ,  $P < 0.001$ ,  $95\% CI = (0.596, 0.830)$ ;  $r_{\text{symbolic}}(62) = 0.567$ ,  $P < 0.001$ ,  $95\% CI = (0.374, 0.714)$ ); see Supplementary Table 1 for non-parametric and robust statistical tests) replicate previous findings<sup>6</sup> but also provide the new result that individual risk attitudes are related to the precision of mental magnitude representations in a way that is robust to sensory noise inherent in specific visual displays. The observed relationship between risk-neutral probability and risk payoff precision was also well-described by the following non-linear formula derived from the NLC model (dotted lines in Fig. 5):

$$\pi = 0.55 \left(1 + \frac{1}{2\sigma^2\gamma^2}\right).$$

This relationship also allowed us to estimate the dispersion of the prior distributions over magnitudes used by the participants, assuming a common prior that was estimated separately for each task ( $\sigma_{\text{non-symbolic}} = 0.366$  and  $\sigma_{\text{symbolic}} = 0.343$ ). The prior dispersion was indistinguishable between the two presentation formats ( $P_{\text{MCMC}} = 0.204$ ) but was substantially lower than the objective prior ( $\sigma_{\text{objective}} = 0.74$  for the risky choice task and  $\sigma_{\text{objective}} = 0.88$  for the perceptual task).

### Risk aversion in financial choices correlates with precision in mental magnitude representation during the independent perceptual task

We tested whether the individual precision of mental magnitude representations generalizes across both perceptual and risky decision-making tasks, and whether risk aversion in the financial choices can thus be predicted by the preceding and fully independent perceptual task. Initial inspection using raw behavioural measures of perceptual accuracy and risk performance already hinted at such a relation, for both display formats (see Extended Data Fig. 7 and Supplementary Table 2 for non-parametric and robust statistical tests). However, raw choice proportions reflect a mix of perceptual and risk sensitivity along with response bias as well as response noise, leaving it unclear which aspect of choice behaviour is driving these relations<sup>31</sup>. We thus used the NLC model to decompose choice behaviour into sensitivity, bias and response noise measures. We first correlated across participants the slopes of the psychometric curves of the perceptual magnitude decision-making task  $\gamma_{\text{perceptual}}$  and the two analogous ‘consistency’ slopes of the two risky-choice tasks  $\gamma_{\text{non-symbolic}}$  and  $\gamma_{\text{symbolic}}$  (see Extended Data Fig. 6a and see Supplementary Table 1 for non-parametric and robust statistical tests). In line with a shared representational mechanism, we found significant positive correlations for both display formats ( $r_{\text{non-symbolic}}(62) = 0.349$ ,  $P = 0.002$ ,  $95\% CI = (0.113, 0.548)$ ;  $r_{\text{symbolic}}(62) = 0.437$ ,  $P < 0.001$ ,  $95\% CI = (0.215, 0.617)$ ). Second, we tested whether individual apparent risk aversion was systematically related to the precision of mental magnitude representations from the separate perceptual task. Indeed, we found significant positive correlations between our measure of perceptual precision  $\gamma_{\text{perceptual}}$  and the risk-neutral probabilities for both types of financial choice  $\pi_{\text{non-symbolic}}$  and  $\pi_{\text{symbolic}}$  (Fig. 5b,  $r_{\text{non-symbolic}}(62) = 0.350$ ,  $P = 0.002$ ,  $95\% CI = (0.114, 0.548)$ ;  $r_{\text{symbolic}}(62) = 0.283$ ,  $P = 0.012$ ,  $95\% CI = (0.040, 0.494)$ ; see Supplementary Table 1 for non-parametric and robust statistical tests). This provides new evidence that common mental magnitude representations are used as basis for both perceptual and economic choices, and that seemingly irrational biases in economic

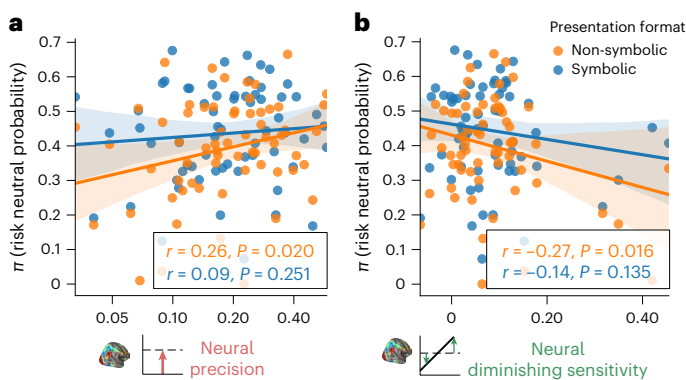


**Fig. 6 | Relationship between neural measures of the precision of magnitude representations and risk aversion.** **a,** Participants with more precise neural magnitude representations ( $n = 64$ ) tended to be less risk averse for the separate financial choices (in particular for non-symbolic presentation format). **b,** Similarly, participants who showed larger neural diminishing sensitivity tended to be more risk averse ( $n = 64$ ). Both findings are in line with the behavioural finding that more risk-neutral individuals perform better on the purely perceptual numerosity task. The shaded area around the regression line represents 95% confidence intervals.  $P$  values were estimated from one-sided Pearson correlations.

choice may in fact be rooted in basic properties of perceptual magnitude representations.

### Risk aversion is related to the precision of neural magnitude representations

Our findings so far indicate that both perceptual and risky financial choices are determined by the noisiness of domain-general magnitude representations that are similarly used across different types of task and visual display. We finally tested to what degree this noise and the ensuing risk aversion in financial choices is also related across purely behavioural and neural measurement techniques, as already shown in the perceptual domain<sup>18,26</sup>. Such a relation would entail that just by measuring the noise in perceptual neural magnitude representations with fMRI, one would already gain information about an individual's risk aversion in future financial choices.

To test this hypothesis, we first examined whether the precision of risky-choice behaviour  $\gamma_{\text{risk}}$  and the risk-neutral probability  $\pi$  were correlated with the precision of the neural magnitude representations in right NPC. While we found no significant correlation between risk precision  $\gamma_{\text{risk}}$  and the neural precision measure for either display ( $r_{\text{non-symbolic}}(62) = 0.122, P = 0.179$ , 95% CI =  $(-0.13, 0.36)$ ;  $r_{\text{symbolic}}(62) = 0.118, P = 0.177$ , 95% CI =  $(-0.13, 0.35)$ ; Extended Data Fig. 6c), we found a significant correlation with neural diminishing sensitivity for non-symbolic payoffs ( $r_{\text{non-symbolic}}(62) = -0.213, P = 0.045$ , 95% CI =  $(-0.44, -0.03)$ ; Extended Data Fig. 6d, orange markers). Correspondingly, for non-symbolic payoffs, risk-neutral probability  $\pi$  correlated significantly with both neural precision ( $r_{\text{non-symbolic}}(62) = 0.258, P = 0.020$ , 95% CI =  $(0.01, 0.47)$ ; Fig. 6a, orange markers) and with neural diminishing sensitivity ( $r_{\text{non-symbolic}}(62) = -0.268, P = 0.016$ , 95% CI =  $(-0.48, -0.02)$ ; Fig. 6b, orange markers). The corresponding correlations for symbolic payoffs were in the same direction but not statistically significant. Thus, we found evidence, albeit less robust across visual display types, that the noisier the neural magnitude representations (neural precision) and the stronger the deterioration of neural representation for larger magnitudes (neural diminishing sensitivity), the more risk averse the individual. This central result was also significant when using non-parametric and robust correlations (see Supplementary Table 3 for more details).

### Effects of neural magnitude precision on individual risk aversion are mediated by noise in mental magnitude representations

Whereas the purely behavioural estimates of magnitude precision were strongly related across all task and display types, the neural and behavioural magnitude representation measures were more strongly related within the perceptual task than across both choice types. This suggests that non-specific noise during the perceptual fMRI measurements (for example, measurement, physiological) may have overshadowed the relationship between neural magnitude precision and risk aversion measured outside the scanner. To account for all our measures using a single integrative framework, we thus performed mediation analyses to test whether risk aversion related specifically to that part of the variance in neural precision that was correlated with behavioural precision. Indeed, the behavioural precision index  $\gamma_{\text{perceptual}}$  significantly mediated ( $\alpha \times \beta$ ) the effect between neural precision and risk aversion (measured as risk-neutral probability  $\pi$ ) for both non-symbolic ( $P_{\text{MCMC}} = 0.014$ ) and symbolic ( $P_{\text{MCMC}} = 0.028$ ) visual displays (Fig. 7a,b). In line with this result,  $\gamma_{\text{perceptual}}$  also significantly mediated the effect between neural precision and risky payoff precision  $\gamma_{\text{risk}}$  for both symbolic ( $\gamma_{\text{non-symbolic}}; P_{\text{MCMC}} = 0.002$ ) and non-symbolic ( $\gamma_{\text{symbolic}}; P_{\text{MCMC}} = 0.003$ ) displays (Extended Data Fig. 8a,b).

For neural diminishing sensitivity, we found no such mediating effects of  $\gamma_{\text{perceptual}}$ , but a significant direct effect ( $c'$ ) on  $\pi$  for non-symbolic payoffs ( $P_{\text{MCMC}} = 0.017$ ) (Fig. 7c,d and Extended Data Fig. 8c,d) and no evidence of an effect for symbolic payoffs. These findings are in line with the significant positive relationship between neural diminishing sensitivity and risk aversion for non-symbolic payoffs (above), which suggests that diminishing sensitivity may capture a latent feature of neural processing that is not fully accounted for by the NLC model. Irrespective of these details, our data provide evidence that neural precision is an aspect of the same latent trait that determines the precision of mental magnitude representations, and that this trait is related to risk aversion after controlling for unspecific noise.

### Discussion

Individual differences in risk aversion have traditionally been thought to emerge from valuation processes, either as a consequence of individual differences in the concavity of the utility curve<sup>1</sup> or as individual 'appetites' for outcome variability<sup>32</sup>. Here we provide direct behavioural and neural evidence for a perceptual account of risk aversion<sup>6,19</sup> proposing that, at least in certain contexts, risk aversion may also arise from systematic biases in the perception of potential payoffs. A crucial prediction of this account is that the degree of risk aversion should be related to the fidelity with which participants perceive numerical magnitudes. In line with this prediction, our results show that both the behavioural acuity of numerosity judgements as well as the fidelity with which the corresponding magnitudes could be read out from neural fMRI activity are mechanistically related to risk aversion in independent risky choices. Notably, the risky choices were taken under very different circumstances, even though the relationship between the neural precision and risk aversion was more pronounced when the presentation format of the payoffs was identical across both tasks (that is, non-symbolic). In addition, we were also able to reproduce previous findings of a topographic numerosity map in parietal cortex<sup>15,23</sup> and its link to numerical perceptual acuity<sup>18</sup>, and we replicated the relationship between magnitude precision and individual risk attitudes within risky choice<sup>6</sup>. These new and confirmatory findings jointly indicate that risk-averse decision-makers may not actually 'shy away from risks' – instead, they may attempt to rationally maximize expected reward, but may be limited in their ability to do so because of cognitive limitations that make them underestimate the larger payoff magnitudes that come with increased risk, just as they also underestimate larger magnitudes in purely perceptual tasks.

Previous work has already sought to understand the link between numeracy and rationality in economic choice<sup>33</sup> and financial

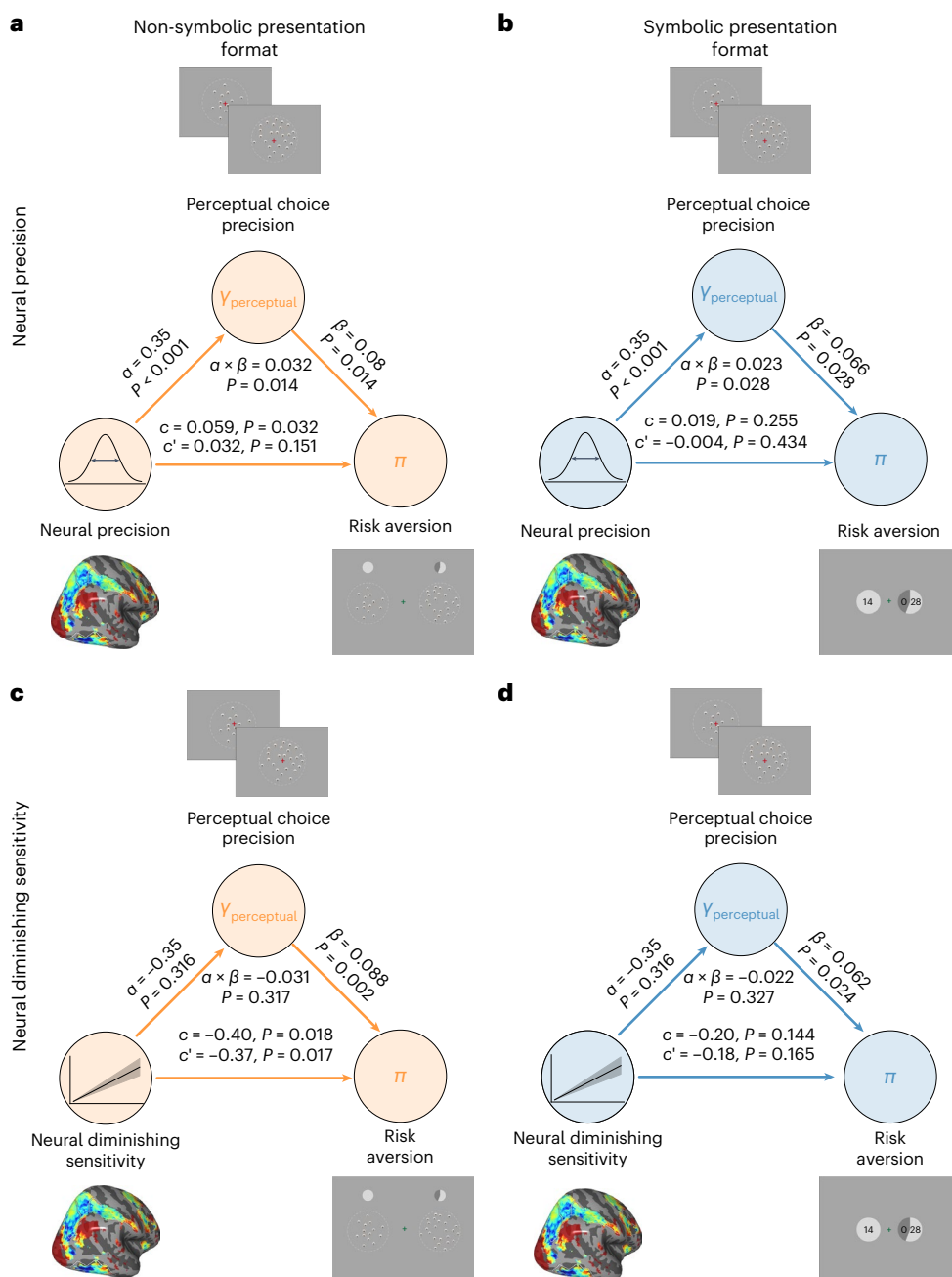


**Fig. 7 | The mediating effect of behavioural magnitude precision reveals the association between neural magnitude precision and risk aversion.** **a,b**, The effect of decoded neural precision on risk aversion ( $n = 64$ ) is significantly mediated by  $\gamma_{\text{perceptual}}$  for non-symbolic (**a**) and symbolic (**b**) presentation formats. **c**, By contrast, there is a direct effect of neural diminishing sensitivity on

risk aversion for non-symbolic payoffs and no mediation effect from  $\gamma_{\text{perceptual}}$ . **d**, This effect was not significant for symbolic payoffs mirroring the correlation pattern in Fig. 6b. One-sided Bayesian  $P$  values were calculated using hierarchical Bayesian mediation analysis (Extended Data Fig. 9b).

decision-making<sup>6,19</sup>, but purely on the basis of behavioural data, without any study of the underlying neurocomputational processes. By applying a unifying, comprehensive computational model rooted in normative theories from perceptual computational neuroscience<sup>34</sup>, we show here how risk aversion may emerge—at least partially—from the precision of neural and mental magnitude representations. These mechanistic links are domain-general not only across differences in visual displays with different sensory noise but also across tasks with different behavioural goals (perceptual accuracy versus maximizing financial value). Our results thus provide evidence that a similar neurocognitive mechanism guides both numerical magnitude perception

and risky choice, suggesting that at least part of the individual differences in risk-averse behaviour can be explained by variability in the acuity of numerical magnitude perception. Therefore, our findings provide direct empirical evidence for a postulated mechanistic link<sup>6</sup> between the interrelated precisions of perceptual and neural magnitude representations<sup>18</sup> and apparent risk aversion.

Our results contribute to an ongoing research programme that seeks to understand the extent to which principles of lower-level perceptual neural processing can account for idiosyncrasies in economic and risky decision-making<sup>6</sup>. Previous neuroimaging work along these lines has so far mainly focussed on characterizing how neural valuation

processes may be constrained by such principles<sup>35</sup>, and investigations of perceptual magnitude coding in parietal cortex had largely been confined to perceptual tasks<sup>14,23</sup>. However, work in psychophysics<sup>36</sup> and on efficient<sup>34</sup> and noisy<sup>13</sup> sensory coding has proposed that seemingly fundamental properties of perceptual processing (for example, Weber's law or regressive bias) may in fact generalize across many task contexts. Recent work has also shown that neurons in inferior parietal sulcus are tuned to represent magnitudes beyond pure numerosities, but more generally across multiple domains such as time intervals<sup>37</sup> and object sizes<sup>16</sup>. This makes it plausible that such psychophysically defined perceptual limitations may also affect behaviour in higher-order cognitive domains, as we show here for risk-taking in the financial domain.

That being said, our results do not imply that individual variability in risky choice solely reflects properties of parietal-encoded mental magnitude representations. Previous studies have identified other sources of neural variability that may relate to individual differences in risky decision-making, such as fluctuations in striatal regions<sup>38</sup> and in anterior insula<sup>39</sup>, or even neural lateralization<sup>40</sup>. More generally, recent findings have also suggested that economic choice variability may be associated with weaker value signals in orbitofrontal cortex<sup>41</sup>. Thus, our results highlight the precision of parietal magnitude representations as just one of several fundamental sources of decision-relevant noise that may lead to individual choice variability and risk attitudes.

In line with the hypothesis of value construction, the brain may flexibly and actively construct subjective value representations from several context-dependent attributes, with noise in magnitude representations being one of the brain features affecting economic choice variability and bias, alongside more affective reward-<sup>38</sup> and value-based<sup>42</sup> neural variability. Generally speaking, the specific mechanisms by which the brain flexibly constructs values may induce the same individual to change their risk attitudes across different contexts. For example, risk-seeking is prevalent in non-human primate studies<sup>43</sup> in which macaques receive feedback of the choice outcome and are rewarded every trial. However, recent work<sup>44</sup> has shown that changing the context of the environment into a more naturalistic, free-range setting can lead non-human primates to behave in a risk-averse manner. Conversely, risk-seeking behaviour is found in humans<sup>45</sup> in experimental models that administer rewards cumulatively. These task design differences could well reflect the brain's flexibility to adapt to changing environments, which may affect the priors, precision and bias in representing monetary offers. Frydman and Jin<sup>19</sup> have shown directly that exposure to different prior distributions of potential payoffs induces changes in risk attitudes. Specifically, more frequent exposure to large numbers induced greater risk-seeking behaviour. Overall, the degree to which individual or contextual choice variability and bias reflects mixtures of perceptual-, reward-, value-based or even emotional processes<sup>46</sup> is thus an exciting question that should be considered in future work.

Our data show that individual differences in behavioural acuity in the perceptual task were more closely correlated with the precision of the neural signal in the right as opposed to left NPC. Similarly, neural diminishing sensitivity for larger numbers—mirroring well-known empirical choice patterns—was more pronounced in right NPC. This apparent right lateralization of the parietal approximate number sense is in line with earlier neuroimaging studies of perceptual numerical magnitude judgement in children<sup>26</sup> and adults<sup>18</sup>. These studies found relationships between behavioural numerical and neural acuity in right IPS but not left IPS—even though the objective numerosity of presented stimuli related to neural activity in both hemispheres. All these findings also align with work in developmental psychology suggesting that number sensitivity in right IPS may potentially represent a more basic number sense that matures very early in life and closely relates to object size processing<sup>16</sup>. By contrast, left IPS function matures throughout childhood and appears more involved in symbolic number processing<sup>26</sup>. Patients with right, but not left, parietal brain damage show impairments in quick numerosity judgements<sup>47</sup>, and a meta-analysis

suggests that the right parietal lobe may be specifically involved in multiplication<sup>48</sup>, the key computational process underlying rational solutions to risky choice.

Our findings that perceptual and neural magnitude noise can mechanistically affect economic choice bias and variability suggest that normative and predictive models such as the NLC can capture basic magnitude representations commonly underlying both risky choice as well as perceptual judgements. However, the current form of the NLC is actually agnostic to whether choices are information-maximizing (that is, perceptual choice) or expected payoff-maximizing (that is, economic choice). Previous results have suggested that models can be set up to explicitly dissociate these two behavioural goals<sup>49</sup>. However, while the NLC may not be as computationally detailed as these more recent optimal coding models, our approach establishes it as one of the few choice models for whom there is an empirical correspondence between model parameters and independent measures of neural processing. This paves the way for other uses of this general approach to validate complex model assumptions, and to predict choice behaviours on the basis of independent measures of basic neural processes.

Our approach of demonstrating that risk-averse behaviour is partially rooted in capacity constraints of perceptual brain processes dovetails with other (neuro)economic choice models that have taken inspiration in neurocomputational accounts of vision, sensory processing, perception, attention or memory, among others<sup>50,51</sup>. Crucially, our specific neurocognitive account of risk aversion illustrates how principled understanding and empirical measurement of basic brain mechanisms may lend credence to choice models that have originally been developed mainly on the basis of theory and/or fits to empirical choice data. Thus, perhaps in analogy to how economic modelling of choice data may benefit from being constrained by choice axioms<sup>52</sup>, our study suggests that the vast space of possible choice models can be narrowed down by empirical measures of the basic information-processing operations assumed by the model. Our approach therefore directly runs counter to previous concerns that the study of brain processes and neural data may provide little information of relevance to knowledge and theories about economic choice<sup>53</sup>. In fact, more recent economic models have already begun to propose cognitive micro-foundations that offer interesting computational hypotheses about choice variability, bias and context-dependent behaviour<sup>6,19</sup>. However, we highlight again that cognitive or economic models that are theoretically based on a neurobiological account should substantiate their assumptions with neural data. This will be essential for disambiguating between the ballooning number of choice models that draw on such theoretical frameworks<sup>54</sup>, and for establishing which of the assumptions underlying these flexible models are in fact plausible in the light of empirical data. For example, empirical evidence from neuroscience suggests various choice constraints that may arise from correlated variability of neuronal populations<sup>55</sup> or from the algorithms the brain uses to flexibly adapt to different choice set sizes<sup>56</sup> or cognitive task space<sup>57</sup>. All such perspectives can provide mechanistic insights that decision theorists and micro-economists may use to advance model-building and therefore develop more neurobiologically grounded accounts of choice behaviour.

Finally, our current results offer correlational evidence of a relationship between mental magnitude representations encoded in parietal cortex and risk-averse behaviour as predicted by the NLC model. We recognize that while we found significant correlations between behavioural measures of perceptual precision and risk aversion, the correlations between our neural precision measures and risk were less robust in certain contexts, such as when payoffs were presented as symbolic numbers. While symbolic and non-symbolic numbers overlap in the way they are encoded in parietal cortex<sup>17</sup>, format-dependence in sensitively decoding magnitude stimuli may possibly account for the differences in explained variance between non-symbolic and symbolic magnitude representations. Our fMRI task model used only non-symbolic numbers to decode

neural magnitude precision because of the mixed results of previous attempts to decode symbolic numbers using multi-voxel decoding fMRI techniques<sup>58</sup>. Future studies could fine-tune better decoding algorithms, develop other numerosity models, or possibly explore other sources of neural data that could reliably decode symbolic numbers from parietal cortex.

Looking ahead, future tests of the NLC model may investigate with brain stimulation methods whether parietal cortex is indeed causally involved in risky decision-making, and to what degree a perceptual account of risky-choice behaviour can be generalized to atypical populations, such as patients diagnosed with dyscalculia<sup>59</sup>, impulse-control disorders<sup>60</sup> and chronic stress<sup>61</sup>. It would also be interesting to map the correspondence between numerical ability and risky-choice behaviour across various stages of human development with dynamic changes of risk attitudes<sup>62</sup>, or even across various real-world contexts with strong differences in risk attitudes, such as in countries with different stages of economic development<sup>63</sup>. Last but not least, our findings may also have policy implications, if it were possible to reliably measure numerical representations in environmental contexts that go beyond controlled laboratory settings. For example, studies on educational outcomes have shown that increasing numeracy has clear long-term consequences in improving financial literacy and lifelong incomes, which may depend on the individual's ability to accurately gauge and evaluate risk<sup>64</sup>.

## Methods

### Participants

Sixty-four right-handed participants (26 females, ages 18 to 35) participated in the study. We informed them about the study's objectives, the equipment used in the experiment, the data recorded and obtained from them, the tasks involved and their expected payoffs. We also screened participants for MR compatibility before their participation in the study. No participant had indications of psychiatric or neurological disorders or needed visual correction. Our experiments conformed to the Declaration of Helsinki and our protocol had the approval from the Canton of Zurich's Ethics Committee.

### Procedure

Participants completed the MRI screening and consent forms on their arrival. They then went into a behavioural testing room and read the instructions for the perceptual magnitude and risky-choice tasks, as well as information on MRI safety. Participants performed two tasks sequentially: a perceptual magnitude task and an economic risky-choice task. Participants completed the perceptual magnitude task inside the MRI scanner, where we recorded their behavioural and neural measures of mental magnitude precision. Participants subsequently completed the risky choice task outside the MRI scanner, inside a behavioural testing room. The order of the tasks was chosen to prevent the statistics of the risky choice task from altering participants' priors and thereby influencing the neural measures of magnitude representation. We also recorded and collected peripheral pupil and physiological measures, specifically eye movements during the perceptual magnitude task. Eye movements were collected using an MR-compatible infrared Eyelink II CL v.4.51 eye-tracker system (SR Research Ltd). After completing both tasks, we paid participants on the basis of both their cumulative score in the perceptual magnitude task and one decision trial randomly selected by our algorithm in the risky choice task (below). We additionally paid a show-up fee of 10 CHF (Swiss francs) for attendance and participation. Participants familiarized themselves with the tasks and performed practice trials of both before they were brought to the MRI scanner room.

### Perceptual magnitude task

Participants had to choose which of two sequentially presented clouds of coins contained a larger quantity of coins. Before the start of every

trial, a red fixation cross was presented for 1 s. Then the first cloud  $C$  was overlaid on the red fixation for 600 ms. After an interval lasting between 6 and 9 s the second set of coin clouds  $X$  appeared on the screen. Only the red fixation remained on the screen during this interval. We chose the presentation timing and interval length in a way that would provide sufficient time to model the haemodynamic response function from neural data, preventing the hemodynamic response of the first stimulus presentation from being contaminated by response-related activity during the second stimulus presentation. The second set appeared for another 600 ms, whereafter the fixation cross changed from red to green, prompting participants to decide within 2.5 s which cloud had the larger quantity of coins. A green-coloured letter 'l' (or 'r') appeared on the screen to indicate participants had pressed left (or right) and thus chose the first (or second) set. Responses made too early (fixation had not turned green) or too late (after 2.5 s and when fixation had reverted back to red) were labelled as missed responses. Each correct response corresponded to a reward of 0.25 CHF, but participants had no feedback on the accuracy of their responses or the accumulation of points throughout the task. The perceptual magnitude task had a total of 216 trials distributed across six runs and lasted a total of 30 to 40 min. The first set varied from 5 to 28, with numbers drawn from a geometric sequence with steps of  $\sqrt{2}$  (5, 7, 10, 14, 20, 28). The second set was constructed by multiplying each magnitude from the first set by a factor of  $2^{h/4}$ , with  $h$  ranging in discrete steps from -6 to 6. Participants were not informed ahead of time what range of magnitudes would be presented to them during the experiment, but the possible payoffs were typical for the types of payoff given for experiments at our laboratory.

### Risky-choice task

Participants had to choose between a certain offer  $C$  and a risky offer  $X$  with a fixed probability  $p = 0.55$ . Thus, a participant choosing the safe option had a 100% chance of being paid  $C$ , but a participant choosing the risky gamble had a 55% chance of being paid  $X$  and a 45% chance of no payment. No feedback of the actual payout outcome occurred throughout the task, but only after the experiment (below). During the task, the monetary payouts were presented in two display formats: symbolic payoffs of Arabic numerals or a cloud of 1-CHF coins. The gambles were presented simultaneously at the left and right sides of the monitor screen. In the beginning of every trial, the stated certain and risky probabilities appeared on the screen alongside the red fixation cross, with the position (left or right from the fixation cross) of these probabilities varying randomly from trial to trial. We used grey-shaded pies to represent the probabilities in both formats. We overlaid numerical monetary offers inside the probability pies when we displayed them as risky symbolic payoffs while we positioned the amounts below the pies when displayed as a cloud of 1-CHF coins. Both display formats were presented in alternating blocks of 40 trials per block, totalling 12 blocks. The monetary amounts were displayed once the fixation cross changed from red to green, and participants had 3 s to choose the gamble on the left or on the right. A green-coloured letter 'l' appeared on the screen when participants pressed left and a green-coloured letter 'r' appeared on the screen when participants pressed right. Responses made too early or too late were missed responses, and these missed trials were not included in the draw of the final trial that determined the monetary payout of the participant.

After participants finished all trials, one trial was randomly drawn for the payout. If on that trial a participant had chosen the certain option, she immediately received that amount. If she had chosen the risky option, she had to roll a virtual 100-sided die. Any result smaller than or equal to 55 was paid out, any other result led to no payout. The task had a total of 480 trials lasting between 30 and 40 min (240 trials per display presentation format). In analogy to the

perceptual task, we determined the monetary payoffs for the sure gamble to vary from 5 to 28, drawn from a geometric sequence with steps of  $\sqrt{2}$ ; the probabilistic lotteries varied by a factor of  $2^{h/4}$  in steps of 0 to 8. Participants were not informed about the range of monetary payouts offered to during the experiment, but the possible payoffs were typical for the types of payoff given for experiments at our laboratory.

### The NLC model

The NLC model assumes that the coding of numerical magnitudes occurs in logarithmic space and the amount of noise of this representation is constant in log space (that is, scale invariant). Thus, the NLC model prescribes that psychometric curves for each stimulus magnitude should have similar slopes when plotted on a logarithmic scale, and that a single psychometric curve can fit all the choice data when plotting the log-ratio of these magnitudes. To this end, we separately fitted six psychometric curves for the perceptual magnitude task, where each curve plots the probability of judging the magnitude  $X$  of the second cloud of coins to be greater than the magnitude  $C$  of the first cloud, as a function of  $X$  and with the reference of each curve being  $C = \{5, 7, 10, 14, 20, 28\}$ . The six psychometric curves for risky choice, on the other hand, represented the probability of choosing the risky gamble with payoff  $X$  over the sure gamble with payoff  $C$ , as a function of  $X$  and with the reference of each curve being  $C = \{5, 7, 10, 14, 20, 28\}$ . To fit the choice data in the perceptual magnitude and risk task, we used the same two-parameter probit model with slope  $\gamma_C$  and intercept  $\delta_C$  in both linear space,

$$\Pr(\text{choose risky}|X) = \Phi(\gamma_C X - \delta_C),$$

and in log space,

$$\Pr(\text{choose risky}|X, C) = \Phi(\gamma_C \log X - \delta_C),$$

where  $\Phi(\cdot)$  is the cumulative distribution function of the standard normal distribution. We separately estimated the parameters,  $(\delta_C, \gamma_C)$  at the population and individual levels using a hierarchical Bayesian framework in RJAGS (Extended Data Fig. 9a).

In a second step, we fitted the NLC with a similar probit model, but now with a single psychometric curve fitted to the choice data of both tasks instead of six separate curves as previously. This version of the model assumes a log-ratio encoding of numerical magnitudes, and we estimated one slope  $\gamma$  and intercept  $\delta$

$$\Pr(\text{choose risky}|X, C) = \Phi\left(\gamma \log\left(\frac{X}{C}\right) - \delta\right).$$

We again measured  $(\delta, \gamma)$  at the population and individual levels. The NLC prescribes that  $\gamma$  measures the precision of our mental magnitude representations while  $\delta$  contains information about the indifference point. We thus constrained the standard probit and rationalized it as the NLC by mapping the probit parameters with NLC model specifications

$$\gamma \equiv \frac{1}{\sqrt{2}\nu}, \quad \delta \equiv \left(\frac{\beta^{-1} \log(p^{-1})}{\sqrt{2}\nu}\right),$$

where  $\nu$  is the noise in mental magnitude representations;  $p$  is the stated probability ( $0 < p < 1$  during risk and  $p = 1$  during perceptual magnitudes) and  $\beta = \frac{\sigma^2}{\sigma^2 + \nu^2}$  is the multiplier that determines the weight of the noisy estimate  $r$  relative to the prior (see ref. 6 for the full derivation).

We can then calculate an individual's indifference point and index of risk aversion using the probit parameters. First, the indifference point is the level at which the individual is indifferent between choosing

either  $X$  or  $C$ , and this indifference is determined by the following threshold rule,

$$\frac{X}{C} = \left(\frac{1}{p}\right)^{\frac{1}{\beta}}.$$

We can derive and estimate the indifference point  $\theta$  using the intercept and slope parameters of the probit formulation of the NLC model during risky choice  $(\delta_{\text{risk}}, \gamma_{\text{risk}})$ ,

$$\theta \equiv \exp\left(\frac{\delta_{\text{risk}}}{\gamma_{\text{risk}}}\right).$$

Second, we can also calculate a standard economic index of risk aversion, namely the risk-neutral probability: the degree to which the probability-of-payoff in the risky-choice options seems to be underestimated. For example, if a participant is so risk averse that her indifference point lies at  $\frac{X}{C} = 3$  (note that an optimal, risk-neutral decision-maker would have the indifference point at  $\frac{X}{C} = \frac{p_{\text{certain}}}{p_{\text{risky}}} = \frac{1}{0.55} \approx 1.82$ ), she chooses equivalent to an optimal risk-neutral decision-maker in the same model if this was set up to contain a  $p = \frac{1}{3}$ . According to NLC, a decision-maker will only behave with a risk-neutral probability equal to the objective probability  $p = 0.55$  in the absence of noise ( $\nu = 0$ ); otherwise, the individual's risk-neutral probability in the presence of noise ( $\nu > 0$ ) is

$$0.55^{\left(\frac{1}{\beta}\right)} \leq 0.55,$$

and, thus, by definition, participants are risk averse. We can similarly derive and measure an individual's risk-neutral probability using the intercept and slope parameters of the probit formulation of the NLC model  $(\delta_{\text{risk}}, \gamma_{\text{risk}})$ ,

$$\pi \equiv \exp\left(-\frac{\delta_{\text{risk}}}{\gamma_{\text{risk}}}\right).$$

Finally, the NLC predicts a positive non-linear relationship between the precision in mental magnitude representations  $\gamma_{\text{risk}}$  and our index of risk aversion  $\pi$ . We fitted a psychometric model that assumes a common prior  $\sigma$  (see Khaw et al.<sup>6</sup> for more details),

$$\pi = 0.55^{\left(1 + \frac{1}{2\sigma^2 \gamma_{\text{risk}}^2}\right)}.$$

We estimated  $\sigma$  by regressing participant precision measures of payoff offers  $\gamma_{\text{risk}}$  to their corresponding risk-neutral probability  $\pi$ . We also fitted the relationship between  $\gamma_{\text{risk}}$  and  $\pi$  using simple linear regression. Given that our central aim was to determine whether individual risk-averse behaviour can be predicted by an independent measure of magnitude precision, we regressed our index of risk aversion  $\pi$  on  $\gamma_{\text{perceptual}}$ .

### Preference-based models

We also fitted stochastic versions of standard economic models to our data to test whether the NLC explains these better than models that explain risk aversion by expected utility maximization. We considered three classes of canonical preference-based models for model comparison, namely (1) constant relative risk aversion, a standard model of expected utility theory<sup>65</sup>; (2) cumulative prospect theory<sup>66</sup> and (3) salience theory<sup>67</sup>. We used probit and logit choice models to account for stochasticity during risky choice. Please see the Supplementary Methods for the exact model specifications used.

### Hierarchical Bayesian parameter estimation

We estimated model parameters using hierarchical Bayesian estimation and Markov chain Monte Carlo (MCMC) techniques<sup>68</sup> using the

Gibbs sampler as implemented in JAGS<sup>69</sup>. We used weakly informative hyperpriors for the group-level distributions.

For every group-level parameter, we also estimated the parameters for each individual participant. These individual-level estimates were drawn from a Gaussian distribution using the mean and standard deviation of the hyperpriors. The exact model specification and used priors can be found in Extended Data Fig. 9. We drew a total of 50,000 burn-in samples to let the MCMC sampler reach a stationary distribution. Then, for each model, we drew a total of 50,000 new samples with three chains each. We sampled each chain using different random number generator engines and different seeds. We thinned the final sample by a factor of 50, thus resulting in a final set of 1,000 samples for each parameter. We used Gelman–Rubin tests to confirm chain convergence of each parameter. All estimated parameters in our Bayesian models showed a  $R < 1.05$ , indicating that all three MCMC chains converged properly. Wherever we wanted to test whether a parameter is larger or smaller than 0, we reported Bayesian *P* values that directly quantify the probability of the reported effect being smaller or larger than zero. We computed these values using posterior population distributions estimated for each parameter. During model comparison, we used the DIC to perform model comparisons<sup>70</sup>.

### MRI acquisition and preprocessing

We acquired functional MRI data at the UZH Zurich Center for Neuroeconomics, using a Philips Achieva 3 T whole-body MR scanner equipped with a 32-channel MR head coil. Specifically, we collected six runs with a T2\*-weighted gradient-recalled echo-planar imaging sequence (189 volumes + 5 dummies; flip angle 90°; repetition time, TR = 2,827 ms; echo time, TE = 30 ms; matrix size 96 × 96, field of view 240 × 240 mm; in-plane resolution of 2.5 mm; 44 slices with thickness of 2.5 mm and a slice gap of 0.5 mm; SENSE acceleration in phase-encoding direction with factor of 1.5; time of acquisition 9:14 min). Additionally, we acquired high-resolution T1-weighted 3D MPRAGE image (field of view 256 × 256 × 170 mm; resolution 1 mm isotropic; inversion time, TI = 2,800 ms; 256 shots, flip angle 8°; TR = 8.3 ms; TE = 3.9 ms; SENSE acceleration in the left to right direction 2; time of acquisition 5.35 min) for image registration during post-processing. Preprocessing was performed fMRIprep v.1.4.0 (ref. 71) using standard settings. For more information on preprocessing and single-trial activation modelling see the Supplementary Information.

### Numerosity encoding model

We used a nPRF( $s$ ) (ref. 72) to model BOLD responses to the first stimulus array. We modelled the data separately for every vertex and for every individual, yielding 36 (six trial-wise regressors per stimulus type per run) activation values for each of the six possible magnitudes of the first stimulus array. We used gradient descent optimization to find a Gaussian receptive field on the logarithmic number line that best predicted number-wise beta estimates in terms of  $R^2$ . The model contained four free parameters: (1) baseline activation  $b$ ; (2) a peak activation  $A$ ; (3) the numerical centre of the logarithmic Gaussian  $\mu$  and (4) the standard deviation of the logarithmic Gaussian  $\sigma$ . All these parameters were jointly estimated using maximum likelihood estimation.

We averaged the vertex-wise parameter estimates over participants by weighting their  $R^2$  and rendered them on the fsaverage6 cortical surface reconstruction using Pycortex. The parameter estimates were thresholded on the mean  $R^2$  across participants at  $R^2 > 0.09$ . This allowed us to qualitatively replicate the topological number fields in the parietal and frontal cortex reported by refs. 15,23 at 3 Tesla, in the group space of a large number of participants ( $n = 64$ ). We manually selected all vertices in and around the IPS<sup>17,18</sup> on the basis of the criteria that the region was both magnitude-sensitive and showed topographic organization. For all participants, we used this same cortical mask, defined as fsaverage6-space.

### Numerosity decoding model

We implemented a Bayesian inversion of the nPRF encoding model,  $f(s)$ , extending on previous work of encoding-decoding models<sup>24</sup>. This allowed us to probe the uncertainty of numerical magnitude representations, operationalized as dispersions of the posterior distributions  $P(s|Y)$ , representing the probability of different numerical magnitudes  $s$ , given the BOLD data  $Y$  of a particular trial. See the Supplementary Information for more details on the exact implementation.

### Individual behavioural and neural variability tests

The hierarchical Bayesian estimation procedure for both behavioural performance during perceptual magnitudes and risky choice produced posterior distributions of NLC model parameters at both population and individual levels. Thus, we extracted the mean of each participant's posterior distribution. On the other hand, our neural encoding and decoding approach was able to extract, on a participant-to-participant basis, a measure of neural precision, which is the inverse of the mean standard deviation (s.d.) of the decoded trial magnitude. We also regressed these standard deviations on the stimulus magnitudes that were presented, to produce a measure of neural diminishing sensitivity that indexes to which extent the acuity of neural representations decreased for larger magnitudes. This measure may be less prone to general noise in the MR data that equally affects all magnitudes. The neural precision had a non-Gaussian distribution because some participants had a precision very close to 0. Therefore, we log-transformed this measure before we ran any correlations. To test for individual differences, we performed simple Pearson correlations and robust regressions. We performed statistical inference on the corresponding parameters using one-sided *P* values, to test the a priori proposed positive relationship between individual behavioural and neural measures as predicted by the model. Any negative correlation would be in the opposite direction to that predicted by the NLC model and our hypothesis and would thus be considered no different from a null effect.

### Bayesian mediation analysis

We used hierarchical Bayesian mediation analysis (Extended Data Fig. 9b) to test whether the individual behavioural magnitude precision  $\gamma_{\text{perceptual}}$  (estimated using the NLC model) mediates the association between our individual neural measurements  $\gamma_{\text{neuro}}$  (neural precision and neural diminishing sensitivity, obtained from our generative encoding and/or decoding model in the perceptual magnitude task) and the individual measurements of risk aversion  $\pi_{\text{risk}}$  and risk precision  $\gamma_{\text{risk}}$ . Similar to previous analyses, we used three chains and the same initial burn-in and thinning steps to obtain a final set of 1,000 samples for each parameter at the population and individual levels. We used Gelman–Rubin tests to check whether all our latent variables had  $R < 1.05$ , which indicated that all three MCMC chains had converged. Finally, we performed inference using Bayesian *P* values, inferred from the highest density interval.

### Reporting summary

Further information on research design is available in the Nature Portfolio Reporting Summary linked to this article.

### Data availability

The behavioural data used in Figs. 2–7 and Extended Data Figs. 2–4, 6, 8 and 9 are available at <https://doi.org/10.5281/zenodo.7966313>. The neuroimaging data are available at Open Neuro: <https://openneuro.org/datasets/ds004259>.

### Code availability

The codes are available at <https://doi.org/10.5281/zenodo.7966313>.

## References

1. Rabin, M. & Thaler, R. H. Anomalies: risk aversion. *J. Econ. Perspect.* **15**, 219–232 (2001).
2. Bruhin, A., Fehr-Duda, H. & Epper, T. Risk and rationality: uncovering heterogeneity in probability distortion. *Econometrica* **78**, 1375–1412 (2010).
3. Kahneman, D. & Tversky, A. Prospect theory: an analysis of decision under risk. *Econometrica* **47**, 263–292 (1979).
4. Mosteller, F. & Nogee, P. An experimental measurement of utility. *J. Political Econ.* **59**, 371–404 (1951).
5. Hey, J. D. Why we should not be silent about noise. *Exp. Econ.* **8**, 325–345 (2005).
6. Khaw, M. W., Li, Z. & Woodford, M. Cognitive imprecision and small-stakes risk aversion. *Rev. Econ. Stud.* **88**, 1979–2013 (2021).
7. Wilcox, N. T. in *Risk Aversion in Experiments* Vol. 12 (eds Cox, J. C. & Harrison, G. W.) 197–292 (Emerald Group Publishing Ltd, 2008).
8. Platt, M. L. & Huettel, S. A. Risky business: the neuroeconomics of decision making under uncertainty. *Nat. Neurosci.* **11**, 398–403 (2008).
9. Roitman, J. D. & Roitman, M. F. Risk-preference differentiates orbitofrontal cortex responses to freely chosen reward outcomes. *Eur. J. Neurosci.* **31**, 1492–1500 (2010).
10. Spitmaan, M., Chu, E. & Soltani, A. Salience-driven value construction for adaptive choice under risk. *J. Neurosci.* **39**, 5195–5209 (2019).
11. Izard, V. & Dehaene, S. Calibrating the mental number line. *Cognition* **106**, 1221–1247 (2008).
12. Nieder, A. & Miller, E. K. Coding of cognitive magnitude. *Neuron* **37**, 149–157 (2003).
13. Petzschner, F. H., Glasauer, S. & Stephan, K. E. A Bayesian perspective on magnitude estimation. *Trends Cogn. Sci.* **19**, 285–293 (2015).
14. Nieder, A. & Dehaene, S. Representation of number in the brain. *Annu Rev. Neurosci.* **32**, 185–208 (2009).
15. Harvey, B. M. & Dumoulin, S. O. A network of topographic numerosity maps in human association cortex. *Nat. Hum. Behav.* **1**, 1424–1434 (2017).
16. Harvey, B. M., Fracasso, A., Petridou, N. & Dumoulin, S. O. Topographic representations of object size and relationships with numerosity reveal generalized quantity processing in human parietal cortex. *Proc. Natl Acad. Sci. USA* **112**, 13525–13530 (2015).
17. Piazza, M., Izard, V., Pinel, P., Le Bihan, D. & Dehaene, S. Tuning curves for approximate numerosity in the human intraparietal sulcus. *Neuron* **44**, 547–555 (2004).
18. Lasne, G., Piazza, M., Dehaene, S., Kleinschmidt, A. & Eger, E. Discriminability of numerosity-evoked fMRI activity patterns in human intra-parietal cortex reflects behavioral numerical acuity. *Cortex* **114**, 90–101 (2019).
19. Frydman, C. & Jin, L. J. Efficient coding and risky choice. *Q. J. Econ.* **137**, 161–213 (2022).
20. Woodford, M. Modeling imprecision in perception, valuation, and choice. *Annu. Rev. Econ.* **12**, 579–601 (2020).
21. Rabin, M. Risk aversion and expected-utility theory: a calibration theorem. *Econometrica* **68**, 1281–1292 (2000).
22. Pouget, A., Beck, J. M., Ma, W. J. & Latham, P. E. Probabilistic brains: knowns and unknowns. *Nat. Neurosci.* **16**, 1170–1178 (2013).
23. Harvey, B. M., Klein, B. P., Petridou, N. & Dumoulin, S. O. Topographic representation of numerosity in the human parietal cortex. *Science* **341**, 1123–1126 (2013).
24. van Bergen, R. S., Ji Ma, W., Pratte, M. S. & Jehee, J. F. M. Sensory uncertainty decoded from visual cortex predicts behavior. *Nat. Neurosci.* **18**, 1728–1730 (2015).
25. Dehaene, S. The neural basis of the Weber–Fechner law: a logarithmic mental number line. *Trends Cogn. Sci.* **7**, 145–147 (2003).
26. Kersey, A. J. & Cantlon, J. F. Neural tuning to numerosity relates to perceptual tuning in 3–6-year-old children. *J. Neurosci.* **37**, 512–522 (2017).
27. Nieder, A., Freedman, D. J. & Miller, E. K. Representation of the quantity of visual items in the primate prefrontal cortex. *Science* **297**, 1708–1711 (2002).
28. van Bergen, R. S. & Jehee, J. F. M. Probabilistic representation in human visual cortex reflects uncertainty in serial decisions. *J. Neurosci.* **39**, 8164–8176 (2019).
29. Wichmann, F. A. & Hill, N. J. The psychometric function: I. fitting, sampling, and goodness of fit. *Percept. Psychophys.* **63**, 1293–1313 (2001).
30. Snoek, L., Miletic, S. & Scholte, H. S. How to control for confounds in decoding analyses of neuroimaging data. *Neuroimage* **184**, 741–760 (2019).
31. Olschewski, S., Rieskamp, J. & Scheibehenne, B. Taxing cognitive capacities reduces choice consistency rather than preference: a model-based test. *J. Exp. Psychol. Gen.* **147**, 462–484 (2018).
32. Gai, P. & Vause, N. Risk appetite: concept and measurement. *Financial Stab. Rev.* **17**, 127–136 (2004).
33. Kacelnik, A. & Brito e Abreu, F. Risky choice and Weber's law. *J. Theor. Biol.* **194**, 289–298 (1998).
34. Wei, X.-X. & Stocker, A. A. A Bayesian observer model constrained by efficient coding can explain 'anti-Bayesian' percepts. *Nat. Neurosci.* **18**, 1509–1517 (2015).
35. Polánía, R., Krajbich, I., Grueschow, M. & Ruff, C. C. Neural oscillations and synchronization differentially support evidence accumulation in perceptual and value-based decision making. *Neuron* **82**, 709–720 (2014).
36. Pardo-Vazquez, J. L. et al. The mechanistic foundation of Weber's law. *Nat. Neurosci.* **22**, 1493–1502 (2019).
37. Harvey, B. M., Dumoulin, S. O., Fracasso, A. & Paul, J. M. A network of topographic maps in human association cortex hierarchically transforms visual timing-selective responses. *Curr. Biol.* **30**, 1424–1434 (2020).
38. Chew, B. et al. Endogenous fluctuations in the dopaminergic midbrain drive behavioral choice variability. *Proc. Natl Acad. Sci. USA* **116**, 18732–18737 (2019).
39. Preuschoff, K., Quartz, S. R. & Bossaerts, P. Human insula activation reflects risk prediction errors as well as risk. *J. Neurosci.* **28**, 2745–2752 (2008).
40. Sacré, P. et al. Risk-taking bias in human decision-making is encoded via a right–left brain push–pull system. *Proc. Natl Acad. Sci. USA* **116**, 1404–1413 (2019).
41. Shi, W., Ballesta, S. & Padoa-Schioppa, C. Neuronal origins of reduced accuracy and biases in economic choices under sequential offers. *eLife* **11**, e75910 (2022).
42. Padoa-Schioppa, C. Neuronal origins of choice variability in economic decisions. *Neuron* **80**, 1322–1336 (2013).
43. Heilbronner, S. R. & Hayden, B. Y. Contextual factors explain risk-seeking preferences in rhesus monkeys. *Front Neurosci.* **7**, 7 (2013).
44. Eisenreich, B. R., Hayden, B. Y. & Zimmermann, J. Macaques are risk-averse in a freely moving foraging task. *Sci. Rep.* **9**, 15091 (2019).
45. Juechems, K., Balaguer, J., Ruz, M. & Summerfield, C. Ventromedial prefrontal cortex encodes a latent estimate of cumulative reward. *Neuron* **93**, 705–714.e4 (2017).
46. Kusev, P. et al. Understanding risky behavior: the influence of cognitive, emotional and hormonal factors on decision-making under risk. *Front. Psychol.* **8**, 102 (2017).
47. Dehaene, S. & Cohen, L. Two mental calculation systems: a case study of severe acalculia with preserved approximation. *Neuropsychologia* **29**, 1045–1074 (1991).

48. Arsalidou, M. & Taylor, M. J. Is 2+2=4? Meta-analyses of brain areas needed for numbers and calculations. *Neuroimage* **54**, 2382–2393 (2011).
49. Heng, J. A., Woodford, M. & Polania, R. Efficient sampling and noisy decisions. *eLife* **9**, e54962 (2020).
50. Polánia, R., Woodford, M. & Ruff, C. C. Efficient coding of subjective value. *Nat. Neurosci.* **22**, 134–142 (2019).
51. Krajbich, I., Armel, C. & Rangel, A. Visual fixations and the computation and comparison of value in simple choice. *Nat. Neurosci.* **13**, 1292–1298 (2010).
52. Caplin, A. & Dean, M. in *Neuroeconomics* (eds Glimcher, P. W. et al.) 21–31 (Elsevier, 2009).
53. Gul, F. & Pesendorfer, W. in *The Foundations of Positive and Normative Economics* (eds Caplin, A. & Schotter, A.) 2–40 (Oxford Univ. Press, 2008).
54. He, L., Zhao, W. J. & Bhatia, S. An ontology of decision models. *Psychol. Rev.* **129**, 49–72 (2022).
55. Haefner, R. M., Gerwinn, S., Macke, J. H. & Bethge, M. Inferring decoding strategies from choice probabilities in the presence of correlated variability. *Nat. Neurosci.* **16**, 235–242 (2013).
56. Furman, M. & Wang, X.-J. Similarity effect and optimal control of multiple-choice decision making. *Neuron* **60**, 1153–1168 (2008).
57. Behrens, T. E. J. et al. What is a cognitive map? Organizing knowledge for flexible behavior. *Neuron* **100**, 490–509 (2018).
58. Lyons, I. M., Ansari, D. & Beilock, S. L. Qualitatively different coding of symbolic and nonsymbolic numbers in the human brain. *Hum. Brain Mapp.* **36**, 475–488 (2015).
59. Price, G. R., Holloway, I., Räsänen, P., Vesterinen, M. & Ansari, D. Impaired parietal magnitude processing in developmental dyscalculia. *Curr. Biol.* **17**, R1042–R1043 (2007).
60. Specker, S., Carlson, G., Christenson, G. & Marcotte, M. Impulse control disorders and attention deficit disorder in pathological gamblers. *Ann. Clin. Psychiatry* **7**, 175–179 (1995).
61. Engelmann, J. B., Meyer, F., Fehr, E. & Ruff, C. C. Anticipatory anxiety disrupts neural valuation during risky choice. *J. Neurosci.* **35**, 3085–3099 (2015).
62. Tymula, A., Rosenberg Belmaker, L. A., Ruderman, L., Glimcher, P. W. & Levy, I. Like cognitive function, decision making across the life span shows profound age-related changes. *Proc. Natl Acad. Sci. USA* **110**, 17143–17148 (2013).
63. Dillon, M. R., Kannan, H., Dean, J. T., Spelke, E. S. & Duflo, E. Cognitive science in the field: a preschool intervention durably enhances intuitive but not formal mathematics. *Science* **357**, 47–55 (2017).
64. Skagerlund, K., Lind, T., Strömbäck, C., Tinghög, G. & Västfjäll, D. Financial literacy and the role of numeracy—how individuals' attitude and affinity with numbers influence financial literacy. *J. Behav. Exp. Econ.* **74**, 18–25 (2018).
65. Apesteguia, J. & Ballester, M. A. Monotone stochastic choice models: the case of risk and time preferences. *J. Political Econ.* **126**, 74–106 (2018).
66. Nilsson, H., Rieskamp, J. & Wagenmakers, E.-J. Hierarchical Bayesian parameter estimation for cumulative prospect theory. *J. Math. Psychol.* **55**, 84–93 (2011).
67. Bordalo, P., Gennaioli, N. & Shleifer, A. Salience theory of choice under risk. *Q. J. Econ.* **127**, 1243–1285 (2012).
68. Kruschke, J. *Doing Bayesian Data Analysis: A Tutorial with R, JAGS, and STAN* (Academic Press, 2015).
69. Plummer, M. JAGS: a program for analysis of Bayesian graphical models using Gibbs sampling. In *Proc. 3rd International Workshop on Distributed Statistical Computing* **124**, 1–10 (2003).
70. Meyer, R. Deviance information criterion (DIC) in *Wiley StatsRef: Statistics Reference Online* (Wiley, 2016); <https://doi.org/10.1002/9781118445112.stat07878>
71. Esteban, O. et al. fMRIprep: a robust preprocessing pipeline for functional MRI. *Nat. Methods* **16**, 111–116 (2019).
72. Dumoulin, S. O. & Wandell, B. A. Population receptive field estimates in human visual cortex. *Neuroimage* **39**, 647–660 (2008).

## Acknowledgements

We are grateful to C. Schnyder, K. Treiber and M. Moisa at the Zurich Center for Neuroeconomics for their excellent assistance in recruitment and participant facilitation. This project has received funding from the European Research Council (ERC) under the European Union's Horizon 2020 research and innovation programme (grant agreement no. 725355, ERC consolidator grant BRAINCODES). M.B.G. was funded by the Marlene Porsche Graduate School in Neuroeconomics and C.C.R. received funding from the University Research Priority Program 'Adaptive Brain Circuits in Development and Learning' (grant no. URPP AdaBD) at the University of Zurich and the Swiss National Science Foundation (grant no. 100019L-173248). G.D.H. was funded by the Dutch Research Council NWO (Rubicon grant no. 019.183SG.017/8O3B). We are thankful for the relevant feedback that we received during the 2019 Sloan-NOMIS Workshop for the Attentional and Perceptual Foundations of Economic Behavior as well as the 2020 virtual Annual Meeting of the Society for Neuroeconomics. The funders had no role in the study design, data collection and analysis, decision to publish or preparation of the manuscript.

## Author contributions

All authors developed the experimental design and procedures, and contributed to the analysis pipeline of the behavioural data. M.B.G. collected the data. M.B.G. and G.D.H. analysed the data. G.D.H. set up the analysis pipeline for the fMRI decoding analysis. M.B.G., G.D.H. and C.C.R. wrote and revised the manuscript, with input from M.G., R.P. and M.W.

## Competing interests

The authors declare no competing interests.

## Additional information

**Extended data** is available for this paper at <https://doi.org/10.1038/s41562-023-01643-4>.

**Supplementary information** The online version contains supplementary material available at <https://doi.org/10.1038/s41562-023-01643-4>.

**Correspondence and requests for materials** should be addressed to Miguel Barreto-García or Christian C. Ruff.

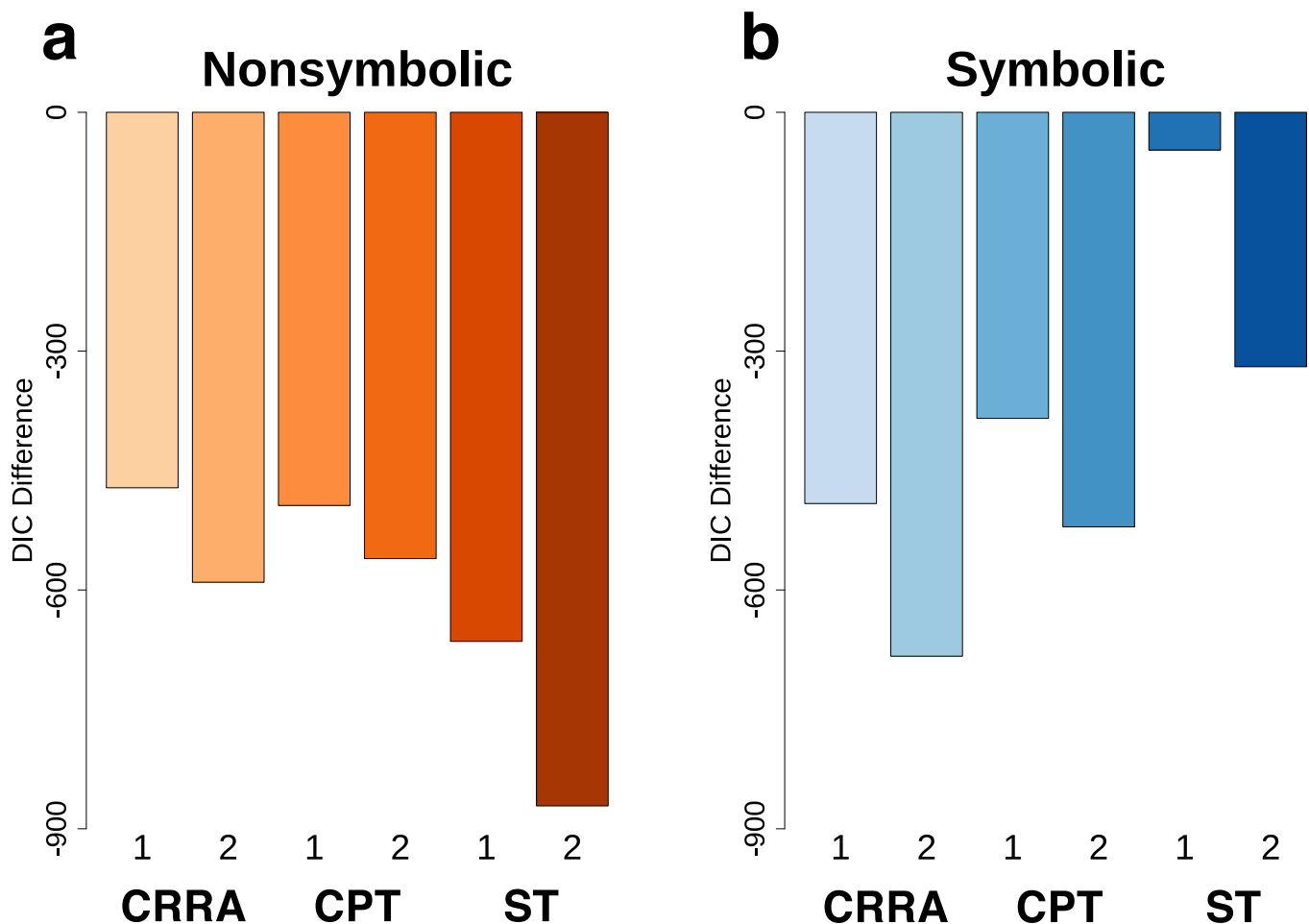
**Peer review information** *Nature Human Behaviour* thanks Colin Camerer, Stefan Glasauer, Ivan Grahek and the other, anonymous, reviewer(s) for their contribution to the peer review of this work. Peer review reports are available.

**Reprints and permissions information** is available at [www.nature.com/reprints](http://www.nature.com/reprints).

**Publisher's note** Springer Nature remains neutral with regard to jurisdictional claims in published maps and institutional affiliations.

Springer Nature or its licensor (e.g. a society or other partner) holds exclusive rights to this article under a publishing agreement with the author(s) or other rightsholder(s); author self-archiving of the accepted manuscript version of this article is solely governed by the terms of such publishing agreement and applicable law.

© The Author(s), under exclusive licence to Springer Nature Limited 2023



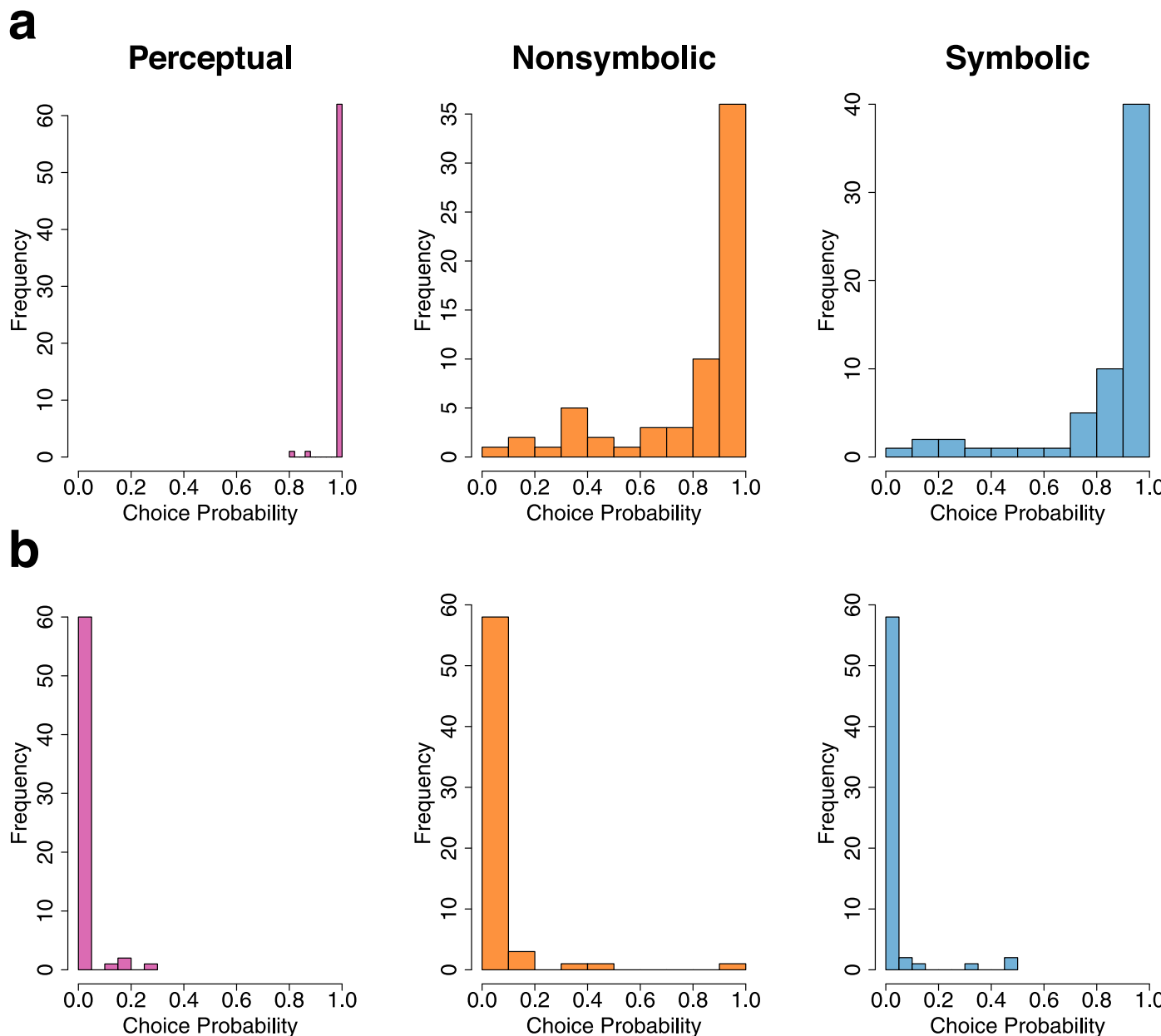
**Extended Data Fig. 1 | Model comparison between the NLC model and competing economic choice models.** DIC difference between the best model (the NLC model in all cases) and the competing economic choice models: constant relative risk aversion (CRRA), cumulative prospect theory (CPT), and

salience theory (ST) in both **(a)** non-symbolic and **(b)** symbolic visual display formats. We fitted each of these economic choice models using the Logit (1) and Probit (2) model specifications.



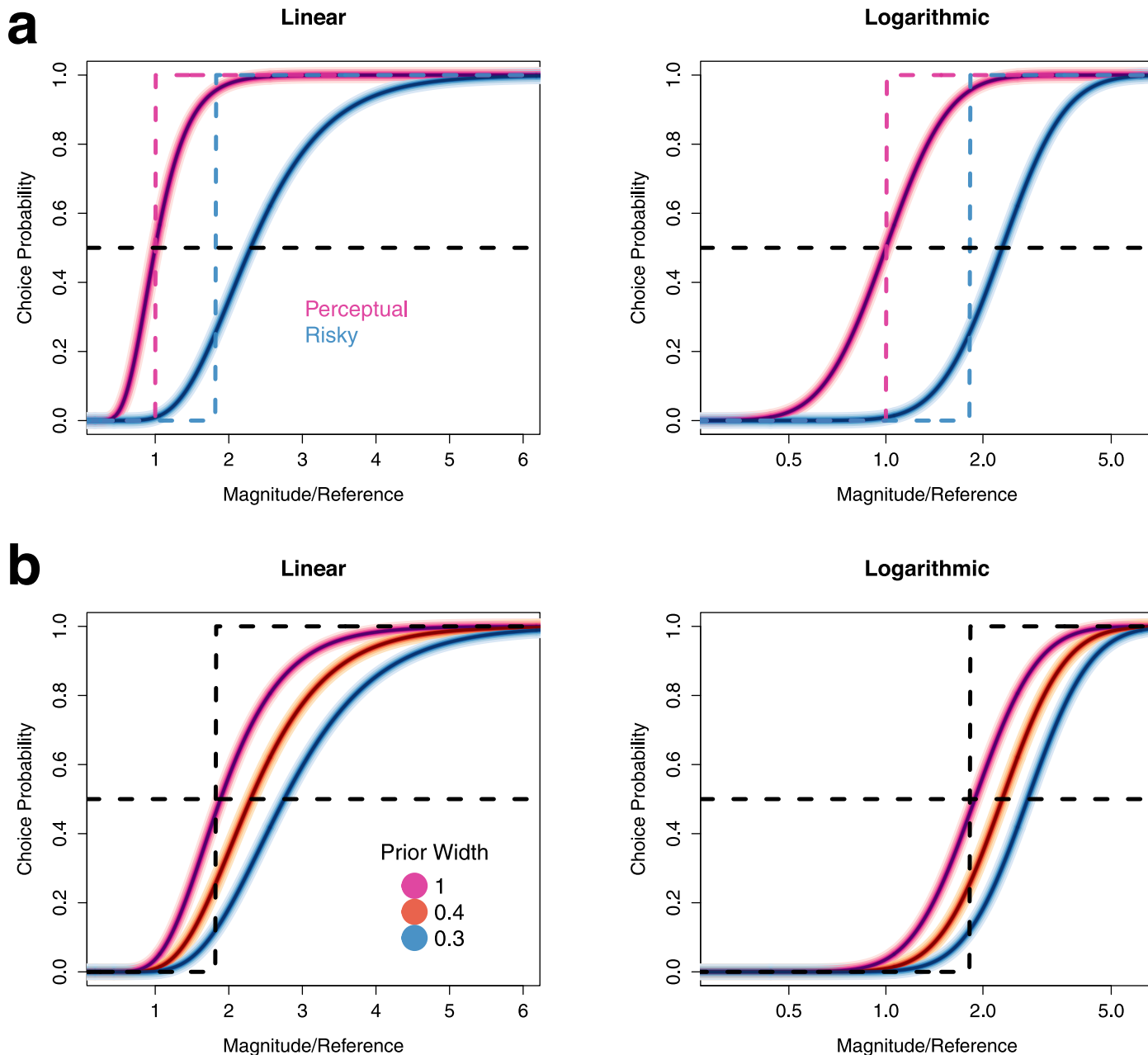
**Extended Data Fig. 2 | Individual behavioural differences.** Observed choice probabilities of each individual participant were plotted against the log-ratio of monetary offers or magnitudes for (a) non-symbolic risky choice (orange), (b)

symbolic risky choice (blue), and (c) perceptual magnitudes (purple). The NLC model was used to fit the psychometric curves of each individual (black solid line). The numbers above each plot denotes participant ID.


**Extended Data Fig. 3 | Individual differences in choices for extreme offer magnitudes.**

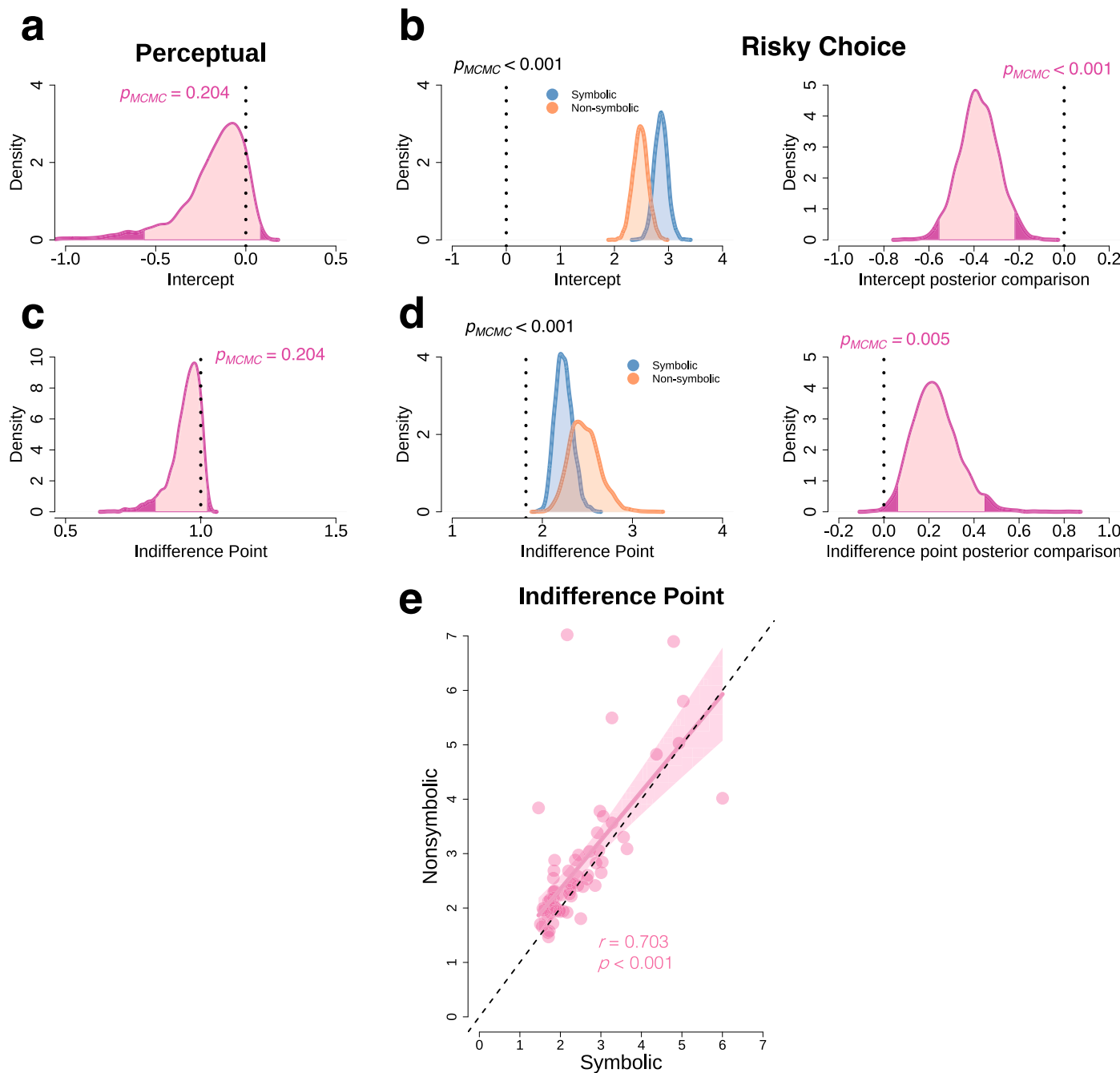
Histograms of choice probabilities (across subjects) for coin clouds (*left, purple*) or risky offers in nonsymbolic (*middle, orange*) and symbolic (*right, blue*) presentation formats, for trials with **(a)** the highest and **(b)** lowest

magnitudes/offers. The distributions are drawn from the extreme value points of the individual choice data in Extended Data Fig. 2. The more the distributions are skewed towards 1 (for **a**) and 0 (for **b**), the less evidence for lapses across individual subjects.



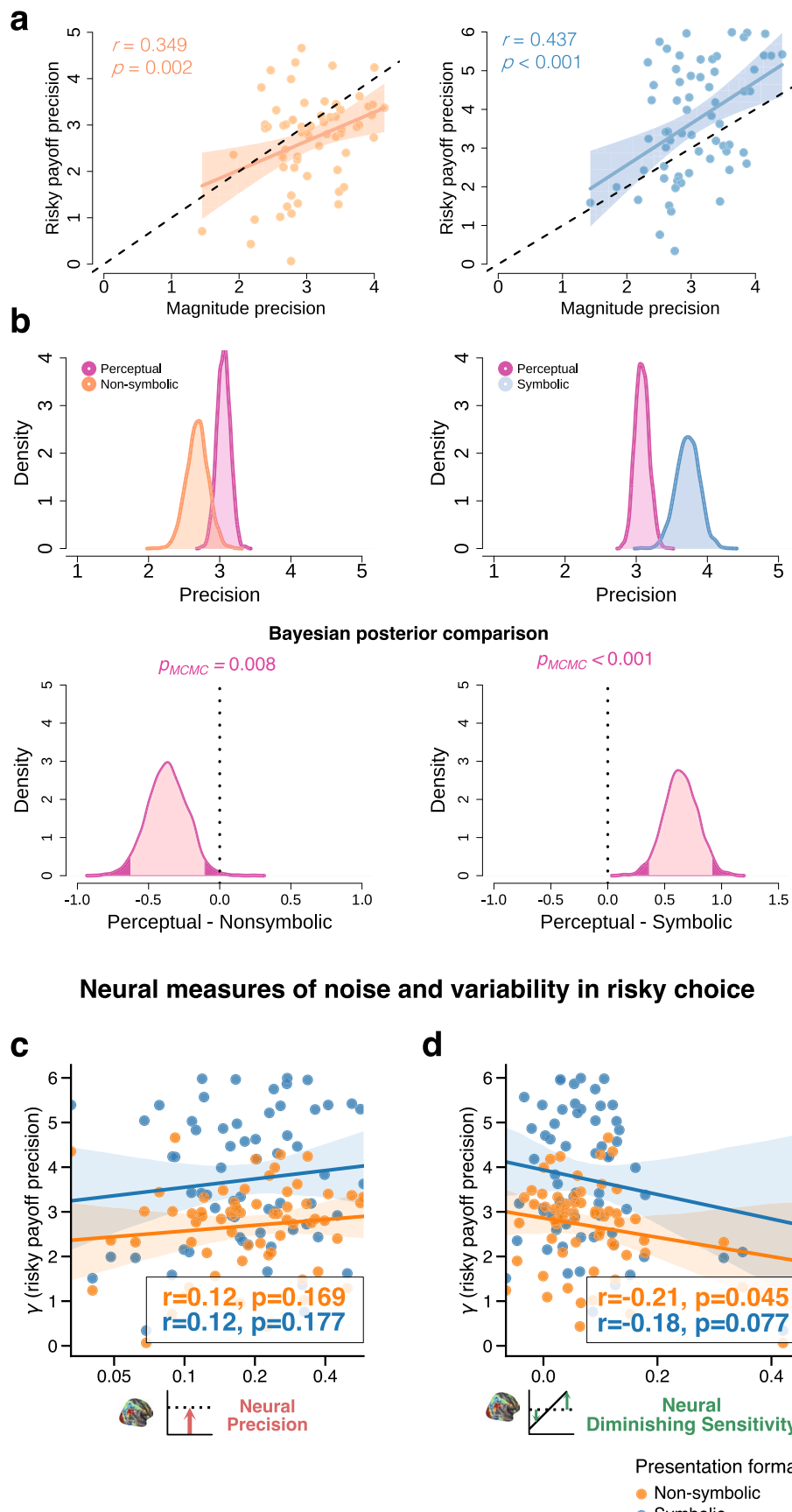
**Extended Data Fig. 4 | The NLC model accounts for perceptual bias and risk aversion arising from noisy magnitude representations.** (a) Choice probabilities plotted in linear (left) and logarithmic (right) space as the ratio of the second- and first-coin cloud magnitudes (perceptual task, red) or risky and sure payoffs (risky-choice task, blue). The NLC model predicts that the indifference point in the perceptual task is  $\theta_{\text{perceptual}} \approx 1$  regardless of noisy magnitude representations while  $\theta_{\text{risky}}$  in risky choice depends on magnitude noise. The indifference point—the ratio of magnitudes where the individual is indifferent between  $X$  or  $C$ , expressed as  $\theta = \left(\frac{1}{p}\right)^{\frac{1}{\beta}}$ —is represented as the intersection of the black horizontal dashed line and the points of the psychometric curve. In perceptual magnitude, there is no outcome uncertainty ( $p = 1$ ) in both dot clouds; hence,  $\theta_{\text{perceptual}} \approx 1$  regardless of whether magnitude representations are noisy ( $\beta < 0$  and  $v > 0$ , solid pink psychometric curve) or not ( $\beta = 1$  and  $v = 0$ , dashed pink stepwise function). This implies that the intercept is  $\delta_{\text{perceptual}} \approx 0$ . In risky choice, outcome probability is fixed at  $p = 0.55$  for the risky payoff. In the absence of noise ( $\beta = 1$  and  $v = 0$ ), the indifference point reflects the relative value of payoffs,  $\theta_{\text{risky}} = \frac{X}{C} = \frac{1}{0.55}$ .

(intersection of the black dashed horizontal line and blue dashed stepwise function). With magnitude noise ( $\beta < 1$  and  $v > 0$ ),  $\theta_{\text{risky}}$  is larger than risk-neutral indifference of  $\frac{1}{0.55}$ ,  $\theta_{\text{risky}} = \left(\frac{1}{0.55}\right)^{\frac{1}{\beta}} > \frac{1}{0.55}$  (intersection of the black dashed horizontal line and blue solid psychometric curve). This is reflected as a shift of the psychometric curve to the right relative to the risk-neutral stepwise function. Risk aversion is quantified as the magnitude of the rightward shift of the psychometric function compared to the risk-neutral indifference point,  $\theta_{\text{risky}} = \frac{1}{0.55}$ . Risk-neutral probability,  $\pi_{\text{risky}}$ , is the reciprocal of the indifference point,  $\pi_{\text{risky}} = 0.55^{\frac{1}{\beta}}$ . (b) Decreasing the width of the prior,  $\sigma$ , shifts the psychometric curve to the right, and thus increases risk aversion. The indifference point can also be expressed as  $\theta = \left(\frac{1}{p}\right)^{\frac{1}{\beta}} = \left(\frac{1}{p}\right)^{\frac{\sigma^2 + v^2}{\sigma^2}}$  to explicitly show the link between  $\sigma$  and  $\theta$ , and why decreasing the prior increases the indifference point and shifts the psychometric curve rightward. The psychometric curves are plotted in linear (left) and logarithmic (right) space and the different colours represent different prior widths.



**Extended Data Fig. 5 | Behavioural effects of the presentation format of monetary magnitudes.** (a) Population posterior distributions of the (a, b) intercept,  $\delta$ , as well as (c, d) the indifference point,  $\theta$ , for both (a, c) perceptual magnitude and (b, d) risky choice tasks. The intercept during perceptual magnitude is no different from zero (indicated here by the vertical dashed line) while it is significantly larger than zero during risky choice in both visual displays. Similarly, the indifference point in perceptual magnitude is no different from one while in risky choice, it is significantly larger than the threshold,  $\frac{1}{0.55}$  (the vertical dashed line). Distributions in pink represent data from the perceptual magnitude task, in blue represent data from risky symbolic payoffs, and in yellow-orange for risky nonsymbolic payoffs. One-sided Bayesian ‘ $p$ -values’ were calculated: The

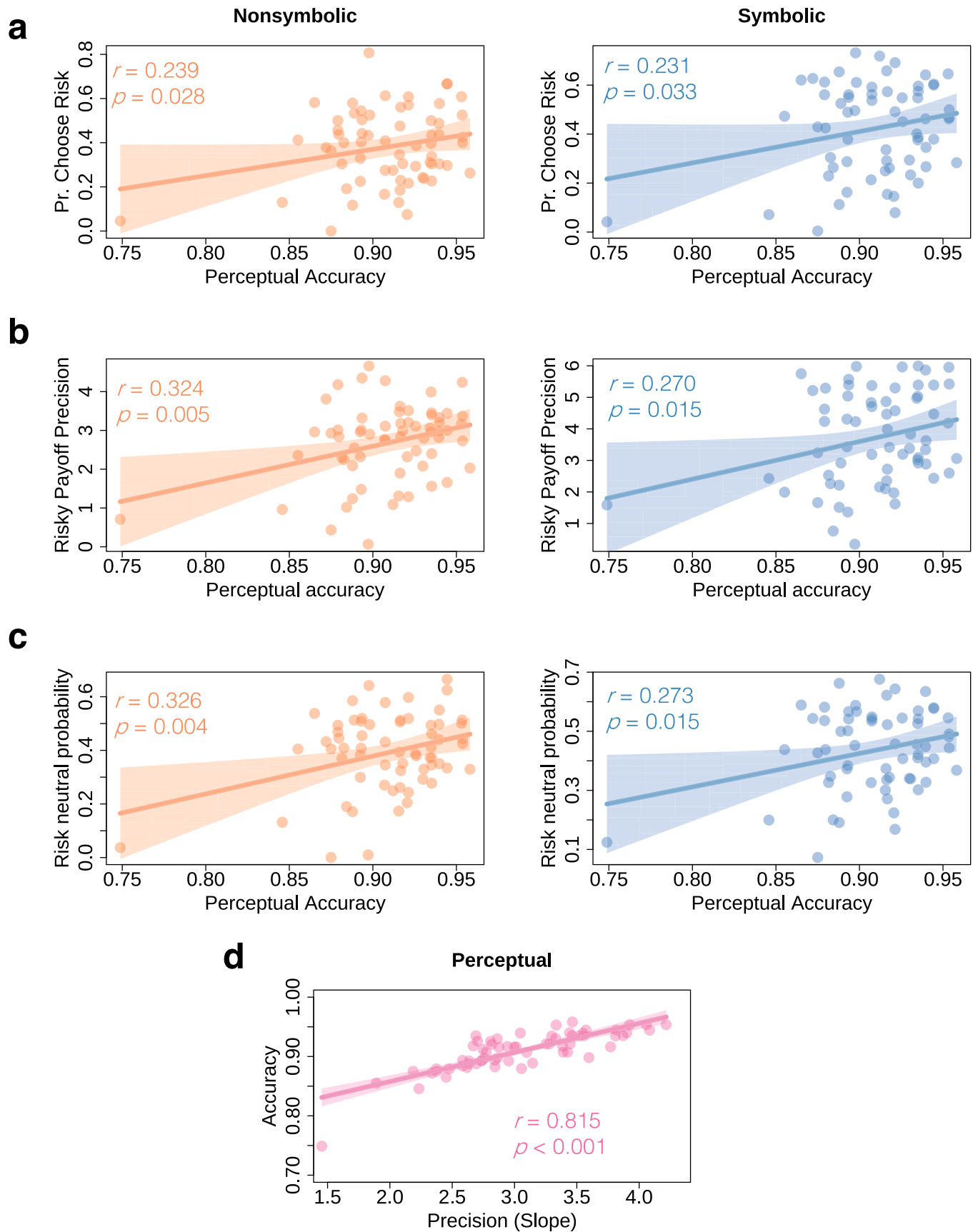
light pink-shaded mass of the highest density interval (HDI) covers 95% of the posterior distribution while the dark-shaded tail-ends represent the most extreme 5% probability mass of the posterior distribution. Bayesian comparison between posteriors reveal that the posterior distribution is significantly different from zero (represented here as a vertical dashed line) if the light-shaded mass does not cross zero. (e) Individual measures of the indifference point for nonsymbolic and symbolic payoffs are positively correlated ( $n = 62$ ). The shaded area around the regression line represents 95% confidence intervals. The black dashed line represents the identity line.  $p$ -values were estimated from one-sided Pearson correlations.



Extended Data Fig. 6 | See next page for caption.

**Extended Data Fig. 6 | Behavioural and neural measures of representation acuity and risky choice variability.** **(a)** The estimated precision of mental magnitude representations employed for the perceptual task,  $\gamma_{perceptual}$ , and the risky decision-making task,  $\gamma_{symbolic}$  and  $\gamma_{nonsymbolic}$ , are related ( $n = 64$ ), for both types of visual displays, as predicted by the NLC model. The diagonal dashed line represents the identity line. Shaded area are error bands corresponding to 95% confidence interval for the regression line.  $p$ -values were estimated from one-sided Pearson correlations. **(b)** Group-level posterior distributions of non-symbolic risk ( $\gamma_{nonsymbolic}$ , orange), symbolic risk ( $\gamma_{symbolic}$ , blue), and perceptual magnitude ( $\gamma_{perceptual}$ , pink) precision. Top plots the posterior distributions while the bottom plots are distributions of differences between precision measurements (in pink). One-sided Bayesian ' $p$ -values' were calculated:

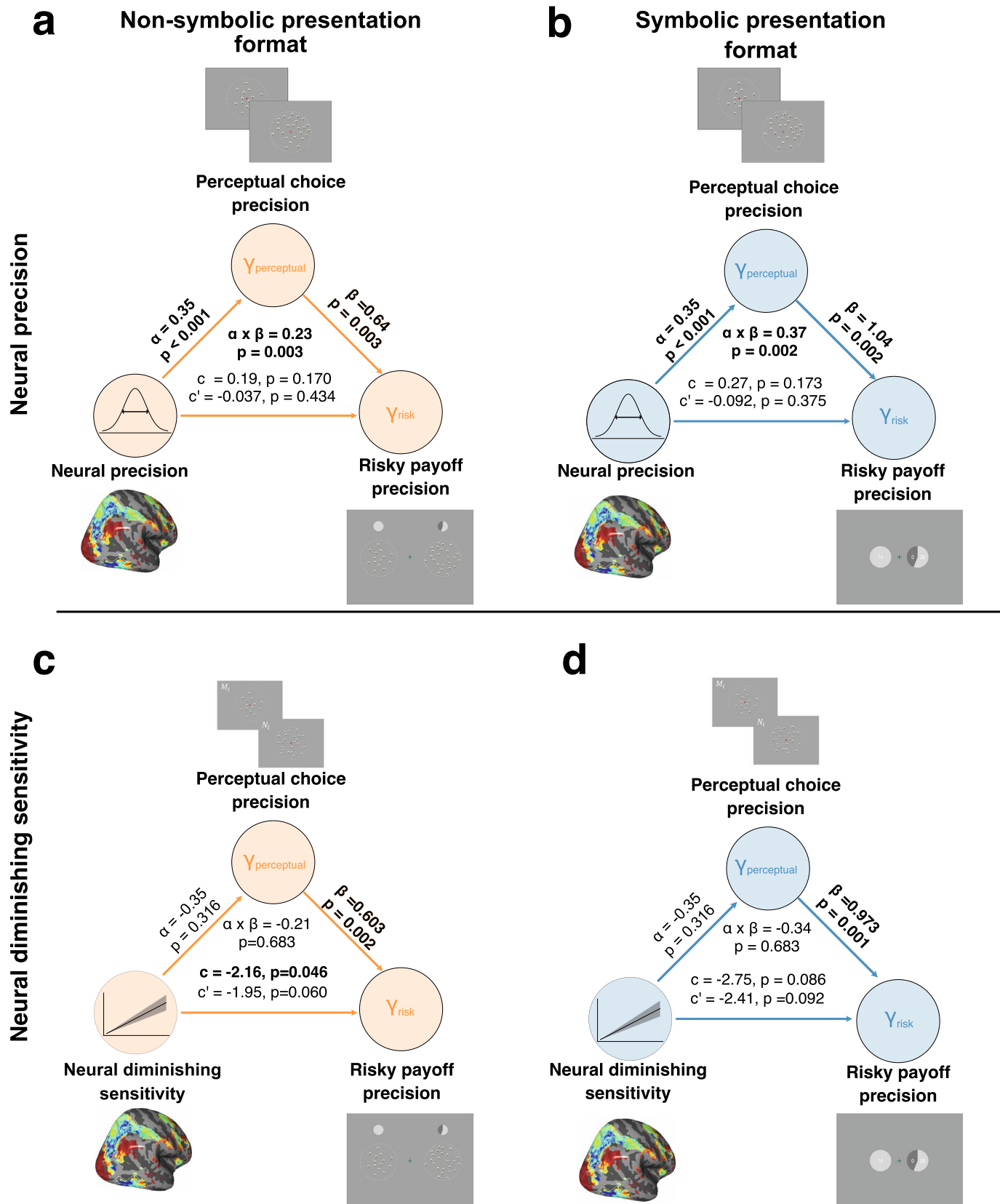
The light-shaded mass of the highest density interval (HDI) covers 95% of the posterior distribution while the dark-shaded tail-ends represent 5% of the posterior distribution. The vertical dashed line represents zero. **(c)** The correlations between the *neural precision* parameter and the risky choice precision parameter  $\gamma$  were not statistically significant ( $n = 64$ ), but in the hypothesised direction: the higher the neural precision, the less variable the behaviour. **(d)** *Neural diminishing sensitivity* was significantly correlated with the risky choice precision parameter  $\gamma$  ( $n = 64$ ) for the non-symbolic presentation format and marginally significant for the symbolic presentation format. The shaded area around the regression line represents 95% confidence intervals.  $p$ -values were estimated from one-sided Pearson correlations.



Extended Data Fig. 7 | See next page for caption.

**Extended Data Fig. 7 | Individual risk measures relate systematically to choice accuracy in the perceptual task.** (a) Raw measures of individual perceptual choice accuracy and the frequency of choosing the risky payoff ( $n = 64$ ) are related across all visual displays. Perceptual accuracy is also related ( $n = 64$ ) to the more precise model-defined measurements of (b) the estimated precision of potential payoffs and (c) the index of risk aversion across visual

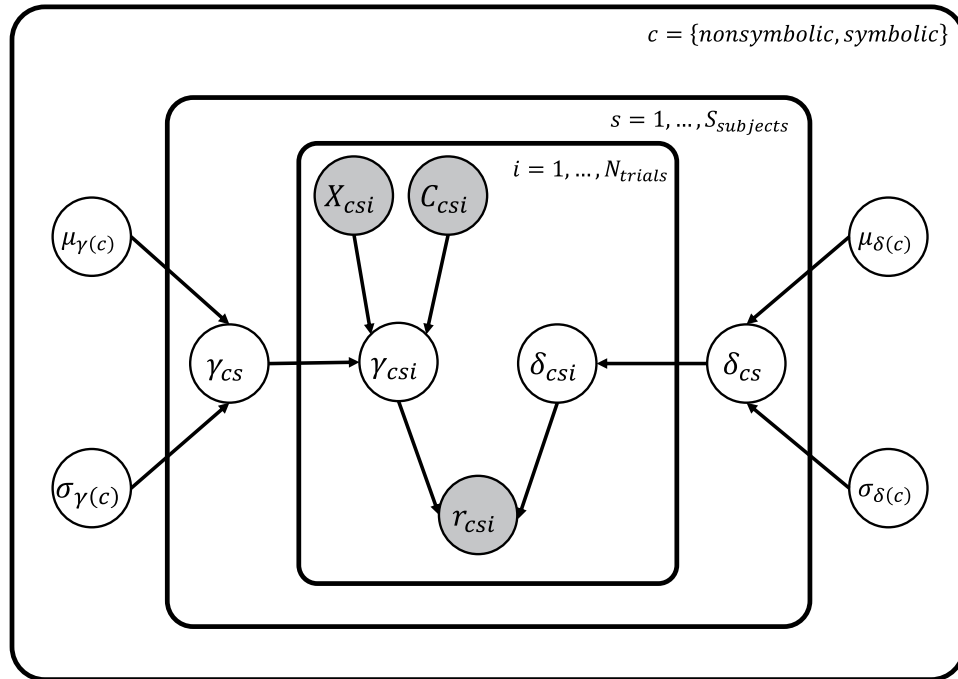
display types. (d) These correlations reflect that magnitude precision in the perceptual task relates strongly to choice accuracy (but is not affected by response biases and the response noise contained in pure choice accuracy measures). Circular dots represent subjects. The shaded area around the regression line represents 95% confidence intervals.  $p$ -values were estimated from one-sided Pearson correlations.



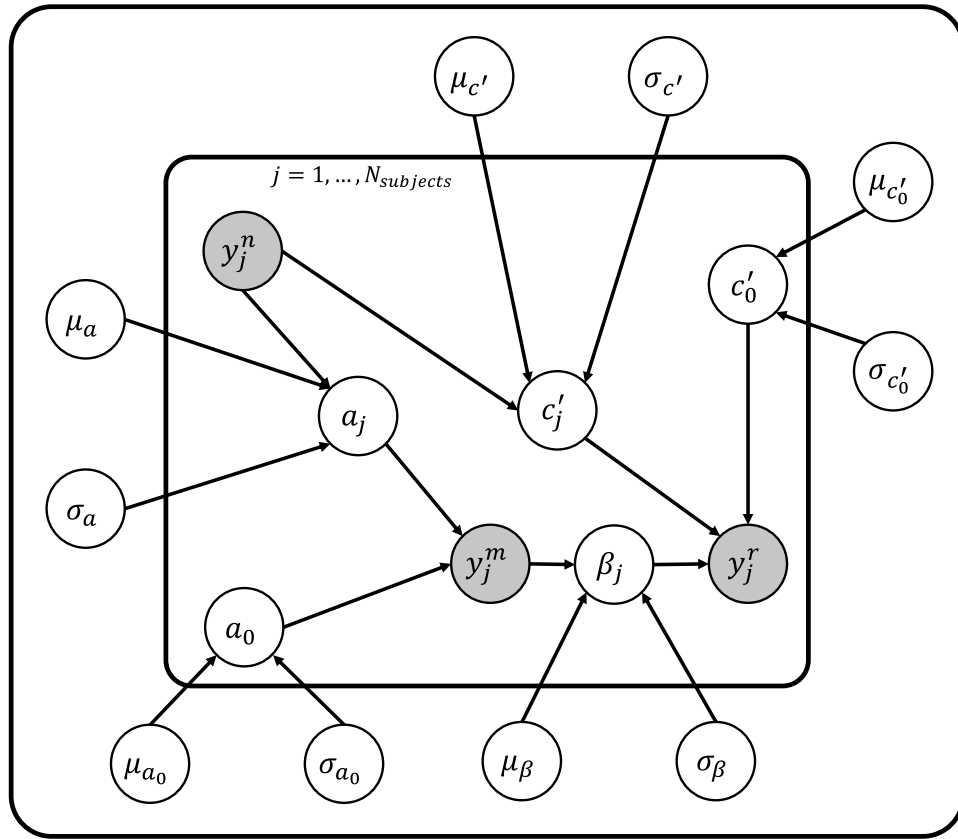
**Extended Data Fig. 8 | Perceptual choice precision mediates the association between neural precision and risky choice precision.** (a) The effect of neural precision on risky choice precision for the task using non-symbolic numbers ( $n = 64$ ) is mediated by perceptual choice variability. There is no significant direct or total effect. (b) The effect of neural precision on risky choice precision for the task using symbolic presentation format is mediated by perceptual choice variability.

There is no significant direct or total effect. The effect of neural diminishing sensitivity on risky choice precision for the task using **(c)** non-symbolic numbers is mediated by perceptual choice precision, but less so for **(d)** symbolic numbers. One-sided Bayesian '*p*-values' were calculated using hierarchical Bayesian mediation analysis (see Methods and Extended Data Fig. 9b).

## a Noisy logarithmic coding model



## b Mediation analysis



**Extended Data Fig. 9 | Hierarchical Bayesian models.** Graphical representations of the hierarchical Bayesian (a) noisy logarithmic coding model and (b) mediation analysis. Clear circles represent latent variables while filled

circles are observed variables, such as trialwise choice ( $r_{csi}$ ) data, subject-wise behavioural and neural measurements ( $y_j$ ), and numerosity/payoff inputs ( $X, C$ ). See Supplementary Note for more details.

## Reporting Summary

Nature Portfolio wishes to improve the reproducibility of the work that we publish. This form provides structure for consistency and transparency in reporting. For further information on Nature Portfolio policies, see our [Editorial Policies](#) and the [Editorial Policy Checklist](#).

### Statistics

For all statistical analyses, confirm that the following items are present in the figure legend, table legend, main text, or Methods section.

n/a Confirmed

- The exact sample size ( $n$ ) for each experimental group/condition, given as a discrete number and unit of measurement
- A statement on whether measurements were taken from distinct samples or whether the same sample was measured repeatedly
- The statistical test(s) used AND whether they are one- or two-sided  
*Only common tests should be described solely by name; describe more complex techniques in the Methods section.*
- A description of all covariates tested
- A description of any assumptions or corrections, such as tests of normality and adjustment for multiple comparisons
- A full description of the statistical parameters including central tendency (e.g. means) or other basic estimates (e.g. regression coefficient) AND variation (e.g. standard deviation) or associated estimates of uncertainty (e.g. confidence intervals)
- For null hypothesis testing, the test statistic (e.g.  $F$ ,  $t$ ,  $r$ ) with confidence intervals, effect sizes, degrees of freedom and  $P$  value noted  
*Give P values as exact values whenever suitable.*
- For Bayesian analysis, information on the choice of priors and Markov chain Monte Carlo settings
- For hierarchical and complex designs, identification of the appropriate level for tests and full reporting of outcomes
- Estimates of effect sizes (e.g. Cohen's  $d$ , Pearson's  $r$ ), indicating how they were calculated

*Our web collection on [statistics for biologists](#) contains articles on many of the points above.*

### Software and code

Policy information about [availability of computer code](#)

#### Data collection

The perceptual magnitude and economic risky choice tasks were both presented and behavioral data were collected using custom-written code in MATLAB R2018a and the Cogent2000 toolbox. The MR-compatible infrared Eyelink II CL v4.51 eye-tracker system (SR Research Ltd.) was used to collect pupil dilation and eye-movement data inside the MRI scanner. The codes for the choice tasks are available at doi: 10.5281/zenodo.7966313.

#### Data analysis

R 3.1.1.1 was used for behavioural and individual-level fMRI modelling and analysis. We used R-JAGS packages for hierarchical Bayesian modeling and mediation analyses (Plummer, 2003). Pre-processing was performed using fMRIprep 1.4.0, which was based on Nipype 1.2.0. Brain tissue segmentation of cerebrospinal fluid (CSF), white-matter (WM) and grey-matter (GM) was performed on the brain-extracted T1w using fast (FSL 5.0.9). Brain surfaces were reconstructed using recon-all (FreeSurfer 6.0.1). Registration was performed with antsRegistration (ANTs 2.2.0). Activation modelling was done via Freesurfer (Fischl et al., 1999). The numerical population receptive field model was rendered on the fsaverage6 cortical surface reconstruction using PyCortex (version 1.2.1). The numerosity decoding model was developed using a Python (version 3.7) package, which is available at (<https://github.com/Gilles86/braincoder/tree/numerosityrisk>). The noise model for decoding was implemented in Tensorflow (version 1.15.5), used gradient descent (Kingma and Ba, 2014).

For manuscripts utilizing custom algorithms or software that are central to the research but not yet described in published literature, software must be made available to editors and reviewers. We strongly encourage code deposition in a community repository (e.g. GitHub). See the Nature Portfolio [guidelines for submitting code & software](#) for further information.

## Data

Policy information about [availability of data](#)

All manuscripts must include a [data availability statement](#). This statement should provide the following information, where applicable:

- Accession codes, unique identifiers, or web links for publicly available datasets
- A description of any restrictions on data availability
- For clinical datasets or third party data, please ensure that the statement adheres to our [policy](#)

The behavioural data are available at doi: 10.5281/zenodo.7966313. The neuroimaging data are available at Open Neuro: <https://openneuro.org/datasets/ds004259>.

## Human research participants

Policy information about [studies involving human research participants and Sex and Gender in Research](#).

### Reporting on sex and gender

We collected participants' data on sex from their MRI screening and consent forms upon their arrival, before the experiment. Information was self-reported and is included in the manuscript. Participant sex was not considered in the design of the experiment and data analysis because we were interested continuous individual differences in perception and risk attitudes, as well as their relation.

### Population characteristics

64 right-handed participants (26 females, ages 18 to 35) volunteered to participate in this study. No participant had indications of psychiatric or neurological disorders or needed visual correction.

### Recruitment

Participants were recruited via the University Registration Study for Study Participants (UAST). All participants were pre-screened for MR compatibility prior to their participation in the study. There is no indication of any self-selection bias during recruitment.

### Ethics oversight

Our experiments conformed to the Declaration of Helsinki and our protocol had the approval from the Canton of Zurich's Ethics Committee.

Note that full information on the approval of the study protocol must also be provided in the manuscript.

## Field-specific reporting

Please select the one below that is the best fit for your research. If you are not sure, read the appropriate sections before making your selection.

Life sciences       Behavioural & social sciences       Ecological, evolutionary & environmental sciences

For a reference copy of the document with all sections, see [nature.com/documents/nr-reporting-summary-flat.pdf](https://nature.com/documents/nr-reporting-summary-flat.pdf)

## Life sciences study design

All studies must disclose on these points even when the disclosure is negative.

### Sample size

64 right-handed participants (26 females, ages 18 to 35) volunteered to participate in this study. Most of the participants were undergraduate and graduate students from the University of Zurich or ETH Zurich. Participants were randomly selected to participate in the study, subject to their MR compatibility. Power analysis was used to calculate the effect size. The sample size was determined based on a power of 0.80 with an alpha of 0.05. Our sample is representative to typical healthy populations with no neurological disorders.

### Data exclusions

No data exclusions.

### Replication

Behavioural results from the study, particularly that of the risky choice task, replicated previous results of a logarithmic encoding and scale invariance of payoff magnitudes from Khaw, et al. (2021, Review of Economic Studies). In particular, we replicated the behavioural results during an initial pilot study and we were able to further replicate the findings from Khaw et al. (2021) in the main study.

### Randomization

Participants performed all the tasks in a within-subject design. Thus, the participants were not allocated to experimental groups and thus randomization was not needed.

### Blinding

No blinding required in this study since this was a within-subjects design. Participants were not grouped to any sort of control or treatment conditions.

## Reporting for specific materials, systems and methods

We require information from authors about some types of materials, experimental systems and methods used in many studies. Here, indicate whether each material, system or method listed is relevant to your study. If you are not sure if a list item applies to your research, read the appropriate section before selecting a response.

## Materials & experimental systems

n/a	Involved in the study
<input checked="" type="checkbox"/>	Antibodies
<input checked="" type="checkbox"/>	Eukaryotic cell lines
<input checked="" type="checkbox"/>	Palaeontology and archaeology
<input checked="" type="checkbox"/>	Animals and other organisms
<input checked="" type="checkbox"/>	Clinical data
<input checked="" type="checkbox"/>	Dual use research of concern

## Methods

n/a	Involved in the study
<input checked="" type="checkbox"/>	ChIP-seq
<input checked="" type="checkbox"/>	Flow cytometry
<input type="checkbox"/>	MRI-based neuroimaging

## Magnetic resonance imaging

### Experimental design

#### Design type

This is an event-related fMRI task design.

#### Design specifications

There were 6 runs and a total of 216 trials during the perceptual magnitude task (36 trials per run) and 480 trials (240 trials each for display presentation format) during the risky choice task. The total experimental session inside the fMRI scanner lasted for 1 hr (30-40 minutes for the perceptual task, 6 minutes for anatomical scan and 10-20 minutes for participant setup) and 30-40 minutes outside the scanner during the risky choice task.

#### Behavioral performance measures

We recorded choices and response times (measured by button presses) as behavioural output measures and related them to variations in the magnitudes presented in the numerosity and risky choice tasks. We evaluated whether participants performed as would be predicted by a psychophysical model of magnitude and risky choice precision (see Khaw et al., 2021). The key measure were the slopes of each individual's choice curves across magnitudes in these tasks, which is an expression of the precision of magnitude representations as specified by the model.

### Acquisition

#### Imaging type(s)

Functional

#### Field strength

3T (Philips Achieva)

#### Sequence & imaging parameters

For each run, we collected T2\*-weighted gradient-recalled echo-planar imaging (GR-EPI) sequence (189 volumes + 5 dummies; flip angle 90 degrees; TR = 2827 ms, TE = 30ms; matrix size 96 × 96, FOV 240 × 240mm; in-plane resolution of 2.5 mm; 44 slices with thickness of 2.5 mm and a slice gap of 0.5mm; SENSE acceleration in phase-encoding direction with factor 1.5; time-of-acquisition 9:14 minutes). We also acquired high-resolution T1-weighted 3D MPRAGE image (FOV: 256×256×170 mm; resolution 1 mm isotropic; TI=2800 ms; 256 shots, flip angle 8 degrees; TR=8.3 ms; TE=3.9 ms; SENSE acceleration in left-right direction 2; time-of-acquisition 5:35 minutes) for image registration during post-processing.

#### Area of acquisition

We used whole brain scans, but optimised the sequence for our region of interest in numerical parietal regions.

#### Diffusion MRI

Used

Not used

### Preprocessing

#### Preprocessing software

We used the fmriprep 1.4.0 preprocessing workflow (<https://fmriprep.org/>).

#### Normalization

All multivariate analyses were performed in individual space, as defined by the 'T1w'-space of fmriprep. The parietal numerosity maps were made via a cortical surface-based registration to the 'fsaverage' surface space of Freesurfer 6.0.1, as included with fmriprep.

#### Normalization template

We used the fsaverage template of Freesurfer 6.0.1 for the visualization of the numerosity maps at the group level and to define the ROI. All decoding analyses were done in individual ('T1w')-space.

#### Noise and artifact removal

The following fmriprep confound regressors were included to correct for scanner (a\_compcor), movement (trans\_x/rot\_x), drift (cosine) and physiological noise (a\_compcor): ['a\_comp\_cor\_00', 'a\_comp\_cor\_01', 'a\_comp\_cor\_02', 'a\_comp\_cor\_03', 'a\_comp\_cor\_04', 'dvars', 'framewise\_displacement', 'cosine00', 'cosine01', 'cosine02', 'cosine03', 'cosine04', 'cosine05', 'cosine06', 'trans\_x', 'trans\_x\_derivative1', 'trans\_y', 'trans\_y\_derivative1', 'trans\_z', 'trans\_z\_derivative1', 'rot\_x', 'rot\_x\_derivative1', 'rot\_y', 'rot\_y\_derivative1', 'rot\_z', 'rot\_z\_derivative1']

#### Volume censoring

We did not apply any volume censoring.

## Statistical modeling & inference

### Model type and settings

We fitted a voxelwise numerical receptive field model as developed by Harvey et al. (2013; 2017) to the parameters estimated in a single-trial GLMs (Mumford et al., 2014). The resulting R<sub>2</sub>s were averaged over subjects and arbitrarily thresholded, just as in Harvey et al.-papers. However, these maps were not used for any statistical inference except visualization and defining a rough anatomy-constrained ROI at the group level by manual segmentation. The resulting estimated encoding models were inverted using the approach pioneered by van Bergen et al. (2015). Crucially, the parameter of the nPRF model were fitted again 6 times, corresponding to 6 hold-out runs. Hence, the estimated predictive accuracy of the decoding model was not biased by "double-dipping".

### Effect(s) tested

No condition-specific effects were tested. We were interested in individual differences across subjects in decoding fidelity rather than condition effects.

### Specify type of analysis:

Whole brain     ROI-based     Both

Anatomical location(s) We focused on the right numerical parietal cortex (NPC) areas previously reported by Harvey et al. (2013; 2017).

### Statistic type for inference (See [Eklund et al. 2016](#))

We did not perform voxelwise statistics and thus did not use the respective inference methods for massively univariate analyses (only multivariate decoding performance).

### Correction

No multiple-comparison correction was performed since no voxel/cluster-wise inferences were made.

## Models & analysis

### n/a Involved in the study

- Functional and/or effective connectivity
- Graph analysis
- Multivariate modeling or predictive analysis

### Multivariate modeling and predictive analysis

Hierarchical Bayesian parameter estimation: we estimated model parameters using hierarchical Bayesian estimation and Markov Chain Monte Carlo (MCMC) techniques (Gelman et al., 2013; Kruschke, 2015). We used a Gibbs sampler implemented in JAGS (Plummer, 2003). We used weakly informative hyperpriors for the group-level distributions. We drew a total of 50,000 burn-in samples to let the MCMC sampler reach a stationary distribution. Then, for each model, we drew a total of 50,000 new samples with three chains each. We sampled each chain using different random number generator engines and different seeds. We thinned the final sample by a factor of 50, thus resulting in a final set of 1,000 samples for each parameter. We used Gelman-Rubin tests to confirm chain convergence of each parameter. All estimated parameters in our Bayesian models showed a  $R < 1.05$ , indicating that all three MCMC chains converged properly.

Numerosity encoding model: we used a numerical population receptive field model (nPRF) (Dumoulin and Wandell, 2008), to model BOLD responses to the first stimulus array. We modelled the data separately for every vertex and for every individual, yielding thirty-six (six trial-wise regressors per stimulus type per run) activation values for each of the six possible magnitudes of the first stimulus array. We used gradient descent optimization to find a Gaussian receptive field on the logarithmic number line that best predicted number-wise beta estimates in terms of R-squared. All these parameters used were jointly estimated using maximum likelihood estimation.

Numerosity decoding model: we implemented a Bayesian inversion of the nPRF encoding model, extending upon previous work of encoding-decoding models (van Bergen and Jehee, 2018; van Bergen et al., 2015). This allowed us to probe the uncertainty of numerical magnitude representations, operationalized as dispersions of the posterior distributions  $\text{Pr}(s|Y)$ , representing the probability of different numerical magnitudes, given the BOLD data of a particular trial type for a particular trial/run.

Model validation: To estimate the robustness of the decoding approach, we evaluated the posterior of unseen data at  $p(s=\{5, 7, 10, 14, 20, 28\})$  to check the mostly likely possible stimulus (maximum a posteriori; MAP stimulus) according to the model. We could then compare the accuracy of the decoding model versus a null model that would perform at chance,  $p(\text{correct})=1/6$  or 16.7%.

Bayesian mediation analysis: we used hierarchical Bayesian mediation analysis to test whether the association between our individual neural measurements (obtained from our generative encoding/decoding model in the perceptual magnitude task) and individual measurements of risk aversion is mediated by individual behavioural magnitude precision (estimated using the NLC model).